

マイコプラズマ・モービル滑走のためにATP合成酵素から進化したモーターの構造

メタデータ	言語: English 出版者: 公開日: 2021-11-10 キーワード (Ja): マイコプラズマ キーワード (En): Mycoplasma 作成者: 豊永, 拓真 メールアドレス: 所属:
URL	https://doi.org/10.24544/ocu.20211111-001

Structure of motor evolved from ATP synthase for

Mycoplasma mobile gliding

(マイコプラズマ・モービル滑走のために ATP 合成酵素から
進化したモーターの構造)

令和 3 年度

Takuma TOYONAGA

(豊永拓真)

CONTENTS

GENERAL INTRODUCTION	...1
CHAPTER I	...5
Chained structure of dimeric F ₁ -like ATPase in <i>Mycoplasma mobile</i> gliding machinery	
CHAPTER II	...44
CryoEM structure of dimeric F ₁ -like ATPase in <i>Mycoplasma mobile</i> gliding machinery	
CONCLUSIONS	...66
ACKNOWLEDGMENTS	...67
REFERENCES	...69

GENERAL INTRODUCTION

Mollicutes

Mollicutes, including *Spiroplasma*, *Mycoplasma* and *Acholeplasma*, are parasitic or commensal bacteria. Many of them are known to cause disease in their host plants and animals. Phylogenetically, they are closely related to *Firmicutes*, which include *Bacillus* and *Clostridium* (1). Mollicutes genomes are small in size (0.5 to 2 Mbp) and their GC content is low (2). They do not have a cell wall, which is composed mainly of peptidoglycans (3). Their cell membrane is surrounded by lipoproteins and other proteins, some of which function as antigenic variations to escape host immune response. Interestingly, in Mollicutes, some *Mycoplasma* species and all *Spiroplasma* species show motilities without flagella or pili that give motility to many bacteria (4-6).

Evolution of Mollicutes motility

Mollicutes have evolved three unique types of motilities: *Spiroplasma* swimming and two types of *Mycoplasma* gliding (Fig. I-1) (7). An evolutionary story is proposed below. Since peptidoglycan is a target of the host cells immune system, Mollicutes abandoned the genes to synthesize peptidoglycan. Accordingly, Mollicutes gave up using flagella, the motility apparatus anchored to the peptidoglycan. Motility is sometimes indispensable in parasitic bacteria, and Mollicutes developed a novel motility that does not require peptidoglycan. Since cells that lose peptidoglycan are soft, as seen in L-form bacteria (8), the cell shape

can be easily deformed by protein movement within the cell. Housekeeping proteins such as the cytoskeletal proteins, ATP synthase, and glycolytic enzymes are constantly moving inside the cell to maintain life. Movements of these proteins are transmitted from the inside of the cell to the scaffold through the membrane, thus resulting in the development of the motilities.

Interestingly, the three developed motilities are completely unrelated in terms of the genes that constitute the motility machinery, and the one type of gliding, represented by *Mycoplasma mobile*, is suggested to have evolved from ATP synthase (5, 9, 10).

ATP synthase

ATP synthases, found in most organisms, are rotary motors that perform biological energy conversion (11, 12). Their role is to both synthesize ATP using a proton motive force and, conversely, to hydrolyze ATP to drive protons to maintain the membrane potential. Their structure is composed of a soluble catalytic F₁-domain for ATP catalysis and a membrane-embedded F_o-domain for the proton pathway (Fig. I-2A). F₁-domain is composed of five subunits α , β , γ , δ , and ϵ , while F_o-domain is usually formed by three subunits a, b, and c. The F₁-domain is also known as F₁-ATPase. For the sake of clarity, I refer to the F₁-domain as F₁-ATPase in this thesis. The smallest unit of F₁-ATPase for their role is $\alpha\beta\gamma$ because it can function by only these subunits (13). The catalytic β and the non-catalytic α subunits alternate to form a hexameric ring ($\alpha\beta$)₃ with a central pore that contains a

coiled-coil domain of γ subunit (Fig. I-2B). The catalytic site is located at the $\alpha\beta$ interface. The three sites in the hexamer cooperate in ATP hydrolysis, and the β subunit adopts the three conformations: Open (O), Closed (C), and Half-Closed (HC) to rotate γ (14).

Mycoplasma have three F₁-like ATPase gene clusters, which are referred to as Type 1 to 3 ATPases (15, 16). Type 1, found in all mycoplasmas, is a typical operon encoding ATP synthase and is likely to function as a proton pump to maintain membrane potential. Type 3 is found in mycoplasmas that have an MIB-MIP system to cleave host immunoglobulins (17). Type 2 is only found in four *Mycoplasma* species, including *M. mobile*. Interestingly, the Type 2 ATPase of *M. mobile*, which encodes MMOB1620, -1630, -1640, -1650, -1660, and -1670 tandemly, is involved in the internal structure of the gliding machinery.

***M. mobile* gliding**

Mycoplasma mobile is one of the mycoplasma species with a cell size of about 0.8 μm and was isolated from a lesion on the gills of a tench (*Tinca tinca*) in the early 1980s (4). *M. mobile* has a protrusion on one side of the cell and glides on solid surfaces at approximately 4 $\mu\text{m/s}$ in the protrusion direction of the protrusion (Fig. I-3A) (5). The gliding machinery is localized to the protrusion and can be divided into surface and internal structures (Fig. I-3B, upper). The surface structure has approximately 450 repeats of a complex of three large proteins, Gli123, Gli521, and Gli349, inserted into the cell membrane (Fig. I-3B, lower) (18-22). Fifty-nm-

long leg structures consisting of Gli349 molecules can be seen jutting out from cell protrusion by electron microscopy (EM) (23). The tip of Gli349 is characterized by a "foot" with an oval structure that can bind to sialylated oligosaccharides (SOs) (24-31). Gli521 and Gli123 serve as the "crank" that transfers force to Gli349 and the "mount" that localizes the other two surface proteins to the gliding machinery, respectively. A working model of the gliding mechanism has been proposed in which the cells are propelled by Gli349 molecules that repeatedly catch, pull, and release SOs on solid surfaces (5, 9, 32, 33).

The internal structure consists of a lumpy structure, called "bell" at the tip of the cell protrusion and 28 "chains" lining the inner membrane surface (Fig. I-3B) (9, 16, 34, 35). Each chain is characterized by 17 repeating particle structures, resulting in a total of 476 particles in one cell. The chains tend to form sheets when they are isolated from cells, suggesting lateral interaction with the adjacent chains (9, 34). The internal structure consists of least ten proteins including MMOB1620, -1630, -1640, -1650, -1660, and -1670 in Type 2 ATPase (Fig. I-3C). Interestingly, MMOB1670 and -1660, which have Walker A and B motifs that are involved in ATP binding and hydrolysis (36), show high amino acid sequence identity with the catalytic β and the non-catalytic α subunits of F_1 -ATPase, respectively. MMOB1670 has an extra N-terminal region (amino acids 1–299), which is not present in the β subunit. The chains most likely contain the motor for gliding because the gliding motility is coupled to ATP hydrolysis (9, 37, 38).

CHAPTER I

Chained structure of dimeric F₁-like ATPase in *Mycoplasma mobile* gliding machinery

ABSTRACT

Mycoplasma mobile, a fish pathogen, exhibits gliding motility using ATP hydrolysis on solid surfaces, including animal cells. The gliding machinery can be divided into surface and internal structures. The internal structure of the motor is composed of 28 so-called “chains” that are each comprised of 17 repeating protein units called “particles”. These proteins include homologs of the catalytic α - and β -subunits of F₁-ATPase. In this study, I isolated the particles and determined their structures using negative-staining electron microscopy and high-speed atomic force microscopy. The isolated particles were composed of five proteins, MMOB1660 (α -subunit homolog), -1670 (β -subunit homolog), -1630, -1620, and -4530, and showed ATP hydrolyzing activity. The 2D structure, with dimensions of 35 and 26 nm, showed dimer of a hexameric ring about 12 nm in diameter, resembling F₁-ATPase catalytic ($\alpha\beta$)₃. I isolated the F₁-like ATPase unit, which is composed of MMOB1660, -1670, and -1630. Furthermore, I isolated the chain and analyzed the 3D structure, showing that dimers of mushroom-like structures resembling F₁-ATPase were connected and aligned along the dimer axis at 31 nm intervals. An atomic model of F₁-ATPase catalytic ($\alpha\beta$)₃ from *Bacillus* PS3 was successfully fitted to each hexameric ring of the mushroom-like structure. These results suggest that

the motor for *M. mobile* gliding shares an evolutionary origin with F₁-ATPase.

Based on the obtained structure, I propose possible force transmission processes in the gliding mechanism.

INTRODUCTION

M. mobile exhibits a unique gliding motility based on ATP hydrolysis on solid surfaces (5). The gliding machinery can be divided into two parts: a surface structure containing legs and an internal structure containing 28 chains that are candidates for gliding motors. The internal chains contain MMOB1660 and -1670, homologs of the α and β subunits of ATP synthase, respectively, suggesting that they evolved from ATP synthase (5).

Recently, the chains of the internal structure were shown to have structural changes linked to ATP hydrolysis (9). However, it is still unclear how the chain generates and transmits the force to the outside, because its detailed structure has not been clarified. In this study, I isolated the chains and elucidated their structures. The structure had a common architecture with F₁-ATPase, suggesting that the chain shares a common evolutionary origin with F₁-ATPase. Based on my findings, I suggest two possible force transmission models for the gliding machinery.

MATERIALS AND METHODS

Strains and culture conditions. I used P476R *gli521*, a mutant strain of *M. mobile* that can glide normally but binds SOs more tightly than wild-type strains (21, 33, 37). *M. mobile* cells were cultured as described previously (39, 40).

Optical microscopy. The cultured cells were inserted into a tunnel chamber assembled with two coverslips and double-sided tapes and observed by phase-contrast microscopy using an inverted microscope (IX71; Olympus, Tokyo, Japan)

(28, 30). Movement was recorded using a complementary metal-oxide semiconductor (CMOS) camera (DMK33UX174; The Imaging Source, Bremen, Germany). Video was analyzed using the ImageJ software, version 1.53a (<http://rsb.info.nih.gov/ij/>).

Solubility test. All procedures for fractionation were performed at 4°C unless otherwise noted and focused protein bands were identified by peptide mass fingerprinting (PMF), as previously reported (34, 41). To investigate the solubility of the chain components, *M. mobile* cells from 60 mL of culture medium were collected by centrifugation at 14000 × *g* for 20 min and washed twice with PBS consisting of 8.1 mM Na₂HPO₄, 1.5 mM KH₂PO₄, pH 7.3, 2.7 mM KCl and 137 mM NaCl. Cells were resuspended in PBS to a 12-fold higher concentration than the culture and sonicated for 1 min at 24–27°C to be dispersed in microtubes using an ultrasonic generator (2510 J-MT; BRANSON, Kanagawa, Japan). The cells were then treated with Triton solution (1% (w/v) Triton X-100, 0.1 mg/mL DNase, 5 mM MgCl₂, and 1 mM phenylmethylsulfonyl fluoride in PBS) in a total volume of 10 mL. After gentle shaking for 1 h, the suspensions were centrifuged at 20000 × *g* for 20 min, and pellets were collected and washed once with suspension buffer (PBS including 5 mM MgCl₂). This fraction is pellet-1. Pellet-1 was then resuspended separately in suspension buffer adjusted to contain different concentrations of NaCl (0, 50, 137, 200, and 400 mM) by pipetting several times. After treatment for 8 h, suspensions were centrifuged at 20000 × *g* for 20 min, and supernatants and pellets collected for SDS-PAGE analysis.

Preparation of fractions. I isolated three fractions including “dimer,” “monomer,” and “chain” structures. They are schematically shown in Fig. I-3B.

For isolation of the dimer, pellet-1 from 1.2-liter culture was resuspended in 5 mL suspension buffer by pipetting up and down and allowed to dissolve for 8 h. The soluble fraction was collected by centrifugation at $20000 \times g$ for 20 min and loaded onto a HiLoad 16/600 Superdex 200 column (Cytiva, Tokyo, Japan) equilibrated with 1 mM $MgCl_2$ in PBS at a flow rate of 0.8 mL/min. The fractions were analyzed by SDS-PAGE and CBB staining.

For isolation of the monomer, pellet-1 from 1.2-liter culture was suspended by 5 mL Tris buffer consisting of 20 mM Tris-HCl (pH 7.5), 250 mM NaCl, 1 mM phenylmethylsulfonyl fluoride, and 1 mM $MgCl_2$ with pipetting and allowed to dissolve for 8 h. The soluble fraction was collected by centrifugation at $20000 \times g$ for 20 min and mixed with 1.5% (w/v) sodium cholate. After 7 h of incubation, the complexes were loaded onto a Sephacryl S-400 HR column (Cytiva) equilibrated with 0.7% sodium cholate, 20 mM Tris-HCl (pH 7.5), 250 mM NaCl, and 1 mM $MgCl_2$ at a flow rate of 0.5 mL/min. The fractions were analyzed by SDS-PAGE and CBB- and reverse-staining (42, 43). The fraction of the complex composed of MMOB1670, -1660, and -1630 was collected. Samples were concentrated using an Amicon Ultra 100 K spin filter (Merck KGaA, Darmstadt, Germany), if necessary.

For isolation of the chain, pellet-1 from 15 mL culture was resuspended in 60 μ L suspension buffer. The suspension was then gently mixed with an equal volume in a suspension buffer adjusted to contain 637 mM NaCl. The chain was recovered

as the supernatant by centrifugation at $5000 \times g$ for 5 min.

Analytical gel filtration. The dimer solution was loaded onto a Sephacryl S-400 HR column equilibrated with gel filtration buffer containing 20 mM Tris-HCl (pH 7.5), 200 mM NaCl and 1 mM $MgCl_2$ at a flow rate of 0.5 mL/min at 4°C.

Thyroglobulin (669 kDa; Gel Filtration Calibration Kits; Cytiva) was dissolved in gel filtration buffer and loaded onto the column as a size standard at a flow rate of 0.5 mL/min. The stoichiometry of protein complexes was estimated by densitometry of SDS-PAGE gels stained with Coomassie brilliant blue (CBB), using a scanner (GT-9800F; Epson, Nagano, Japan) and ImageJ (20).

Blue-native PAGE and in-gel ATPase activity assays. Blue-native (BN) PAGE was performed according to the user manual of the Native PAGE Novex Bis-Tris Gel System (Thermo Fisher Scientific, Waltham, MA). For BN-PAGE of sodium cholate treated dimer, a dimer fraction was mixed with sodium cholate (1.5%) and incubated at 4°C for 9 h. When this sample was mixed with a sample buffer, NativePAGE™ 5% (w/v) G-250 sample additive was also added at 0.5% (w/v) to prevent protein aggregation. Thyroglobulin was dissolved in water and used as a negative control for the In-gel ATPase activity assay. For the In-gel ATPase activity assay (44, 45), native gels were incubated with gentle shaking for 8 h at 24–27°C in activity buffer containing 270 mM glycine, 35 mM Tris (pH 8.4), 4 mM ATP, 14 mM $MgSO_4$, and 0.2% (w/v) $Pb(NO_3)_2$. The gels were rinsed once with water and images were taken using LAS-4000 mini (Cytiva). White precipitates were then dissolved by gentle shaking for 8 h at 24–27°C with 50% (v/v) methanol and 10%

(v/v) acetic acid in water. The gels were restained with 0.025% (w/v) CBB G-250 and 10% acetic acid in water for 80 min at 24–27°C with gentle shaking and destained with 10% (v/v) ethanol and 10% acetic acid in water for 180 min at 24–27°C with gentle shaking. The gels were rinsed once with water and images were taken using LAS-4000 mini.

Phosphate-release assay. Dimer solution was dialyzed for 8 h using 20 mM Tris-HCl (pH 7.5), 150 mM NaCl, and 2 mM MgCl₂. ATPase activity was assayed by a continuous spectrophotometric method using a 2-amino-6-mercapto-7-methylpurine ribonucleoside–purine nucleoside phosphorylase reaction to detect released inorganic phosphate (EnzChek kit; Thermo Fisher Scientific) (46). The reaction mixture was as follows: 15.7 nM dimer, 20 mM Tris-HCl (pH 7.5), 150 mM NaCl, 2 mM MgCl₂ and 0.01–1 mM ATP in a total volume of 0.2 mL at 25°C. Sodium azide was added to 15.4 mM final concentration when the reaction was started. The protein amount of the MMOB1670 comprising F₁-ATPase β-subunit homologs was estimated using densitometric analysis of SDS-PAGE gels.

Negative-staining EM and image processing. Dimer solution was placed on a glow-discharged (PIB-10; VACUUM DEVICE, Ibaraki, Japan) carbon-coated grid (F-400; Nisshin EM Co., Tokyo, Japan) and incubated for 1 min at 24–27°C. The solution was then removed, and the grid was stained with 2% (w/v) uranyl acetate for 30 s. The stain was then removed, and the grid was air-dried. To observe the monomer and chain, the grids were washed with water after 1 min of incubation and then treated as described for the dimer solution. Samples were observed using

a transmission EM (JEM1010; JEOL, Tokyo, Japan) at 80 kV, equipped with a FastScan-F214 (T) charge-coupled-device (CCD) camera (TVIPS, Gauting, Germany), and images were captured at 2.58 Å/pixel.

The contrast transfer function parameters for electron micrographs were estimated using Gctf (47). Further image processing was performed using RELION 3.0 (48). A total of 2148 particles for the dimer and 11687 particles for the monomer were automatically selected with box sizes of 180 × 180 and 100 × 100 pixels using reference-based auto-picking, respectively. These particle images were binned to 5.16 Å/pixel. For the dimer, the particle images were 2D-classified into 100 classes. For the monomer, particle images were 2D-classified in four rounds, and the selected 7381 particles were re-extracted with the pixel size returned to the unbinned image and then 2D-classified into 50 classes.

For reconstruction of the 3D chain structure, 2127 particles were manually selected for chains with a box size of 276 × 276 pixels with ~50% overlap. These particle images were binned to 5.16 Å/pixel. Particle images were 2D-classified in two rounds, and the selected 1709 particles were used to reconstruct the initial model with a final resolution limit of 50 Å. The initial model and selected particles were used to perform 3D refinement. Reprojection images were produced from the 3D map using the `relion_project` command in RELION. The 3D map was visualized using UCSF Chimera 1.14 (49). Atomic models of F₁-ATPase catalytic (αβ)₃ from *B. PS3* (PDB ID 6N2Y) (50) were fitted into the 3D map using command of “Fit in map” in UCSF Chimera.

High-speed atomic force microscopy. Imaging was performed with a laboratory-built tapping mode high-speed atomic force microscopy (HS-AFM) (51, 52), using small cantilevers (BLAC10DS-A2, Olympus; resonant frequency, ~0.5 MHz in water; quality factor, ~1.5 in water; spring constant, ~0.1 N/m). The cantilever's free-oscillation peak-to-peak amplitude (A_0) and set-point amplitude were set at ~2.5 nm and $\sim 0.8 \times A_0$, respectively. The probe tip was grown on the original tip end of a cantilever through electron beam deposition and further sharpened using a radio frequency plasma etcher (PE-2000, South Bay Technology, Redondo Beach, CA) under an argon gas atmosphere (typically at 180 mTorr and 15 W for 3 min). The sample was deposited on a freshly cleaved mica disc glued to a glass stage beforehand. After 3.5 min, the stage surface was immersed in a liquid cell containing an observation buffer [20 mM Tris-HCl (pH 7.5), 50 mM KCl, and 2 mM $MgCl_2$]. Imaging was performed at 24–27°C. AFM images were processed using a low-pass filter to remove spike noise and make the xy -plane flat and analyzed using Kodec software (version 4.4.7.39) (53). Surface profiles and smoothing were performed using ImageJ software.

RESULTS

Isolation and biochemical analyses of stable unit complex. In this study, I isolated and analyzed three fractions including “dimer,” “monomer,” and “chain” structures which are schematically shown in Fig. I-3B (Fig. I-4,5).

First, to isolate a stable unit complex from the chain, I lysed cultured *M. mobile* cells with 1% Triton X-100 and recovered the insoluble fraction by centrifugation (34). This fraction named as “pellet-1” was used for further preparations (Fig. I-4). I suspended pellet-1 in suspension buffer, which contains 137 mM NaCl, and solubilized the putative unit complex for 8 h. Here, I used 137 mM NaCl rather than 400 mM to reduce the contamination of other proteins. The soluble fraction was then subjected to Superdex 200 gel filtration chromatography. The obtained peak fraction in the void volume contained MMOB1620, -1630, -1660, and -1670, which are coded on the mycoplasma Type 2 ATPase operon, and MMOB4530 annotated as phosphoglycerate kinase (PGK) (Fig. I-6A). These proteins are known to be components of the internal structure (Fig. I-3B) (9, 16, 34, 35).

To examine the assembly of these proteins, I applied the isolated fraction to gel filtration chromatography using a Sephacryl S-400 HR column, which can fractionate up to 8000 kDa globular proteins (Fig. I-6B). The proteins eluted as a single peak at a nonvoid position and were larger than 669 kDa, suggesting that they form a large complex. The molar ratios of the components were estimated to be 3.2: 2.9: 3.0: 1.0: 2.3 for MMOB1670, -4530, -1660, -1630, and -1620, respectively, from the relative intensity of the SDS-PAGE bands. I then analyzed the isolated fraction by BN-PAGE (Fig. I-6C, left). A single band was detected, which is consistent with the result of gel filtration chromatography showing a single peak. Next, I applied the band to an In-gel ATPase activity assay, which detects the activity as a white precipitation of lead caused by released of inorganic phosphate

(Fig. I-6C, right). The band with the complex showed precipitation, whereas the band with thyroglobulin, the negative control, did not. This result indicates that the isolated complex has ATPase activity.

In addition, I assayed the isolated fraction for phosphate release from solution. The complex hydrolyzed ATP at a maximum turnover rate of 0.18 molecules/s per MMOB1670 subunit, β -subunit homolog, with a K_m of 74 μ M at 25°C (Fig. I-6D). The ATPase activity was inhibited by addition of 15.4 mM sodium azide, an inhibitor to ATPases with Walker A motifs (54), with a K_m of 108 μ M and a maximum turnover rate of 0.055 molecules/s. In a previous study, the Triton-insoluble fraction, which included the internal structure, showed ATPase activity with a K_m of 66 μ M and a maximum turnover rate of 0.09 molecules/s and was suppressed by 15.4 mM sodium azide, showing a K_m of 84 μ M and a maximum rate of 0.063 molecules/s (9). The values obtained here are comparable to these previous data. The above results suggest that the isolated complex is the motor in the internal structure of the gliding machinery. I used this unit complex for further analyses.

Hexamers resembling F₁-ATPase catalytic ($\alpha\beta$)₃ form a dimer. I observed the unit complex by EM using the negative-staining method. A field image showed uniform particles with dimensions of 40 and 20 nm (Fig. I-7A and B). As the appearance frequency of the particle depended on the protein concentration, I concluded that the observed particles were a part of the protein complex. I picked 2148 particle images automatically using RELION software (48) for 2D-classification. From the 2D-classification, I obtained four clear particle images (Fig.

I-7C). I adopted mirror images according to the structure observed in HS-AFM (see below). Structural handedness cannot be judged from EM images because they are projections of electrons transmitted through the sample. I focused on an image showing a complex structure with dimensions of 35 and 26 nm featuring nearly two-fold symmetry (Fig. I-7C and D). Interestingly, the characteristic hexamer of about 12 nm in diameter formed a dimer and was reminiscent of F₁-ATPase catalytic ($\alpha\beta$)₃. Considering that the amino acid sequences of MMOB1660 and -1670 have high identity to the α - and β -subunits of F₁-ATPase, respectively, the dimeric complex is likely an evolutionary related F₁-ATPase. The distance between the centers of the two hexamers was 11.0 nm. The complex had ten filamentous structures around the two hexamers, four of which appeared to form bridges across the two hexamers. The filamentous structures are unlikely artifact, because they showed common features in four independent averaged images (Fig. I-7C). Hereafter, I refer to this structural unit as a “dimer.”

The hexamer featured a ring and a peak in HS-AFM of a dimer. Next, I visualized the dimer using HS-AFM to clarify the structure under liquid conditions, because the molecules are in dry condition under negative-staining EM. HS-AFM is a powerful method that can visualize the structure and dynamics of single molecules in liquid conditions at a video rate (55, 56). In this method, a specimen is placed on the stage surface and, with a probe, is scanned in buffer at high speed. In this study, I placed a dimer on a mica surface and scanned it in an area of 70 × 70 nm² at 56 × 56 pixels with a scanning rate of 100 ms per frame. HS-AFM

images showed a complex with dimensions of approximately 30 and 20 nm composed of two globules and attached by 2 to 4 lateral protrusions shorter than 15 nm (Fig. I-8A). The dimer images were categorized into two patterns as either a ring (pattern I) or a peak (pattern II), based on the central parts of two globules. Then, I observed them at a higher resolution (area, $40 \times 40 \text{ nm}^2$ with 50×50 pixels; scanning rate, 100 ms per frame) (Fig. I-8B). In pattern I, the slice image near the top end of the particle between 9.8 and 11.3 nm above the substrate surface showed two hexameric rings (Fig. I-8C). The position and direction of the two rings are consistent with those of the hexamers in the negative-staining EM image. In addition, the distance between the centers of the two hexameric rings was 10.4 nm (Fig. I-8D), similar with the distance between the centers of the hexamers in the negative-staining EM image (Fig. I-7C). These observations suggest that the shape of the dimer structure in liquid is preserved in negative-staining EM conditions and that the hexamers form rings like F_1 -ATPase catalytic $(\alpha\beta)_3$. In pattern II, the two central peaks were positioned 11.2 nm apart (Fig. I-8D, lower), similar to the distance between the centers of the hexameric rings in pattern I (Fig. I-8D, upper), suggesting that patterns I and II are two sides of the same coin (Fig. I-8A, left). The distances between the hexameric rings are slightly different for patterns I and II, at 10.4 and 11.2 nm, respectively. This difference suggests that the central axes of two hexamers are not parallel. Considering that HS-AFM detects surface structures while EM shows projection images, the corresponding distance, 11.0 nm in EM is consistent with the numbers obtained from HS-AFM.

Interestingly, in most of the particles, the two peaks at 5 and 6 nm became invisible in 20 s, between frames 1 and 3 (Fig. I-8E and F). I concluded that these subunits dropped out from the complex, because they did not reappear before the complex was disrupted. Next, I focused on the lateral protrusions of these particles, which may be related to the sheet formation of chains (9). To visualize them more clearly, I scanned a dimer by HS-AFM with an area of $120 \times 120 \text{ nm}^2$, 120×120 pixels, and scanning rate 500 ms per frame. The dimer showed seven lateral protrusions around the two globules (Fig. I-8G). These protrusions swayed without being fixed (Fig. I-8H).

Isolation and structure of a monomer. To clarify the components and structure of the hexamer, I focused on the monomeric hexamer, called a monomer (Fig. I-5, left). I treated the dimer fraction with 1.5% sodium cholate, an anionic detergent. BN-PAGE and In-gel ATPase activity assays showed a single band with ATPase activity at a position lower than the original one, corresponding to 720 to 1048 kDa, indicating that the dimer dissociated into smaller units with ATPase activity (Fig. I-6C). Therefore, to isolate a monomer, I applied pellet-1 sequentially to the treatments with 250 mM NaCl for 8 h, 1.5% sodium cholate for 7 h, and to Sephacryl S-400HR gel filtration chromatography (Fig. I-5). The elution pattern showed a rather isolated small peak and following overlapping peaks (Fig. I-9A). An SDS-PAGE gel showed that MMOB1670, -1660, and -1630 eluted in the same fractions, while MMOB4530 and -1620 eluted at later fractions (Fig. I-9), indicating that MMOB4530 and -1620 were dissociated from the dimer by sodium cholate

treatment. Then, I focused on the small peak fraction, F6 in Fig. I-9A, which mainly contained MMOB1670, -1660, and -1630 (Fig. I-5, left, I-9B). MMOB4530 was also contained in F6, but its amount was 9-fold lower than that of the dimer fraction (Fig. I-5, left and middle). The complex in F6 presumably corresponds to the BN-PAGE band showing ATPase activity (Fig. I-6C), because only MMOB1660 and -1670 have the Walker A and Walker B motifs in the dimer components.

EM observation using the negative-staining method showed uniform globular particles 10–15 nm in diameter (Fig. I-10A and B). As the appearance frequency of the particle depended on the protein concentration, I concluded that the observed particles were a part of monomer. I picked 11687 particle images automatically using RELION software for 2D-classification. By 2D-classifying the images in 50 classes, I obtained 15 clear particle images, which were averaged (Fig. I-10C). Fig. I-10D shows a 12 nm diameter globule characterized by a single hexameric ring, corresponding to a part of the dimer image in Fig. I-7C. Three of the subunits were larger than the others with hook structures on either side of the edge. Three averaged images (II to IV) showed a mushroom-like structure resembling F₁-ATPase, which is characterized by a 12 nm-diameter umbrella and a 3 nm-long stalk (Fig. I-10D). Now, I can suggest that MMOB1670, -1660, and -1630 form a monomer, i.e., F₁-like ATPase unit. MMOB4530 was probably not included in this unit because it probably binds to the complex and could not be distinguished in the image due to the low proportion of bound entities (Fig. I-5, left). Thus, the hexameric ring is likely formed by the α -subunit homolog MMOB1660 and the β -

subunit homolog MMOB1670, and the stalk is formed by MMOB1630.

Isolation and structure of a chain. In gliding machinery, dimers link to form chains. To characterize these chains, I isolated “chain fraction” with milder mechanical treatment than those for other fractions. Pellet-1 was treated by 387 mM NaCl, and soluble fraction was isolated. The chain fraction contained more than 30 proteins, including the dimer component proteins MMOB1670, -4530, -1660, -1630, and -1620 as major components (Fig. I-5, right). EM observation using the negative-staining method showed chain structures with lengths longer than 70 nm and particles of various sizes (Fig. I-11A and B). This time I manually picked 2127 particles from the chain images, overlapping approximately 50% of the $71 \times 71 \text{ nm}^2$ box area. From 2D-classification, I obtained seven clear particle images (Fig. I-11C). The particle images show the various orientations required for 3D reconstruction. I then created a 3D map by combining a total of 1709 particle images of good quality (Fig. I-11D). The 3D map with dimensions of 70, 20, and 15 nm at a density threshold (contour level = 0.026) was composed of two dimers of mushroom-like structures resembling F_1 -ATPase, aligned along the dimer axis. Dimers were connected by a bulge structure with a diameter of 5 nm. The chain interval was 31 nm, consistent with the corresponding dimension in a 2D image from electron cryotomography (ECT) (9), suggesting that the 3D model obtained reflects the original structure from a cell. The mushroom-like structure with a diameter of 15 nm, consisting of a hexameric ring and a central stalk, was connected to the dimer by two bridge structures with a diameter of 3 to 6 nm. An

atomic model of F₁-ATPase catalytic ($\alpha\beta$)₃ from *Bacillus* PS3 (PDB ID 6N2Y) (50) was fitted into each hexameric ring of the mushroom-like structure (Fig. I-11E). The distance between the centers of the fitted ($\alpha\beta$)₃ in the dimer was 12.5 nm, which is consistent with that of the dimer observed by negative-staining EM and HS-AFM (Fig. I-7C and I-8D). The fitted model showed that each hexameric ring had two protrusions of 3 to 6 nm pointing laterally (Fig. I-11E). The cross-sections of each mushroom-like structure showed the central stalk length of 5 nm (Fig. I-11F). A cavity was observed at the center of the hexameric ring. However, it may be an artifact of the low-resolution map of negative-staining EM, because metal coating tends to emphasize the peripheral part of large particles (57).

Next, I compared a reprojection image of the 3D chain map with the 2D averaged image of the dimer from negative-staining EM in corresponding handedness (Fig. I-11G). Two short filaments marked by asterisks in the dimer (Fig. I-11G, left) are positioned facing each other in the connecting bulge (Fig. I-11G). Previously, ECT of a permeabilized *M. mobile* cell showed a chain structure characterized by repeats of two globules and two types of projections to the cell membrane (Fig. I-11H, left) (9). The hexameric ring and the central stalk in the 3D map here correspond to the globule and one type of projection to the cell membrane in the ECT image, respectively, suggesting that the chain is oriented with the central stalk facing the membrane, which is common in F₁-ATPases. At the interface between dimers, the 3D map here did not include a structure composed of another type of projection and a globule as observed in the ECT image. The

subunits corresponding to these structures probably had structural variations or dissociation during the isolation process.

DISCUSSION

Outline of internal structure of gliding machinery. Previously, sequence analysis suggested that the chain of *M. mobile* gliding machinery evolved from F₁-ATPase (5, 9, 16, 34, 35). The present study supports this conclusion by structural data showing that the chain has hexameric rings similar to the F₁-ATPase catalytic ($\alpha\beta$)₃. Integrating available information, I can now describe the outline of the internal structure of *the M. mobile* gliding machinery (Fig. I-3B). *M. mobile* cells have 28 individual 530 nm long chains, each of which contains 17 dimer units composed of two F₁-like ATPases and filamentous structures (9). The central stalk of the F₁-like ATPase and another protrusion from the connecting bulge project to the cell membrane.

Unique role of F₁-ATPase related complex. To date, several complexes are known to be evolutionarily related to F₁-ATPase, all of which are responsible for transporting substances across the membrane (58). However, the motor I identified here most likely plays a role in motility. This case may be reminiscent of dynein, a motor in eukaryotes, which evolved from a widely conserved AAA (ATPases associated with diverse cellular activities)+ protein, in which multiple subunits of ATPases perform functional rotation (59, 60). Sequence analyses have shown that

mycoplasma Type 3 ATPase is also related to F₁-ATPase, and its role has been suggested to promote substrate turnover in the MIB-MIP system (17). If Type 3 ATPase provides the force to change the conformation of a hydrolytic enzyme, its role in force generation is common with Type 2, the gliding motor.

ATP synthases are known to be dimerized through interactions between F_o-domains and are usually arranged in rows along the short axis in the tightly curved cristae ridges of mitochondria (12, 61, 62). The dimer structure found in the present study is not related to this, because the F₁-like domain (F₁-like ATPase) is dimerized through the filament structure and is linked in the long axis direction. However, the role of their dimerization may be common, in part, if the dimerization and chain formation observed in the gliding motor identified in this study stabilizes the membrane structure, as seen in the ATP synthase dimer (63). Moreover, dimerization may result in cooperativity in motor functions.

Protein assignment. The α -subunit homolog MMOB1660 (58.7 kDa) and the β -subunit homolog MMOB1670 (88.4 kDa) likely correspond to the smaller and larger subunits, respectively, of the hexameric ring of an F₁-like ATPase unit, as suggested by the estimated 1:1 molar ratio in the dimer (Fig. I-5A, right and I-10D). This means that the hook structure of the larger subunit may be formed by the extra N-terminal region (34.8 kDa) of MMOB1670.

MMOB1630 has only 16.4% amino-acid identity in 336 residues with the γ subunit, the principal component of the central stalk of F₁-ATPase in *Bacillus* PS3. However, 3D structure modeling based on secondary structure suggested that

MMOB1630 is structurally similar to the γ subunit (5). In general, the γ subunit of F_1 -ATPase is composed of a coiled-coil and a globular domain and penetrates the hexameric ring (14). In the F_1 -like ATPase unit and chain 3D model, a stalk structure, suggesting the globular domain of the γ subunit, was found in the center of the hexameric ring (Fig. I-10D and I-11F), implying that MMOB1630 penetrates the hexameric ring like the γ subunit.

Using HS-AFM observations, the peak at approximately 5 nm at the center of the hexameric ring dropped out with time (Fig. I-8E). The peak height agrees with the length of the estimated globular domain of MMOB1630 in the chain 3D model (Fig. I-8F and I-11F), suggesting that the peak is composed of MMOB1630 and was pulled out from the hexameric ring by the scanning cantilever during HS-AFM observation. The pull-out event is thought to be common to that of the F_1 -ATPase, in which the γ subunit is removed from the hexameric ring by optical tweezers (64). The filamentous structures around the hexameric ring probably correspond to lateral protrusions in the HS-AFM images and are formed by the remaining proteins, MMOB1620 and -4530 (PGK). These proteins probably play roles in ATPase dimerization, chain formation, and lateral chain interaction (9). MMOB1620 is an unannotated protein specific to the Type 2 ATPase gene cluster (15, 16). MMOB4530 is annotated as an enzyme that transfers phosphate groups from 1,3-bisphosphoglycerate to ADP in glycolysis to yield ATP and 3-phosphoglycerate (65). In *M. mobile*, ATP is probably provided by glycolysis (66). MMOB4530 may supply ATP efficiently to the gliding motor by its close proximity. Yeast V-ATPase,

which belongs to the rotary ATPase family like ATP synthase, is also attached by two glycolytic enzymes, 6-phosphofructo-1-kinase and aldolase (67-69). These glycolytic enzymes are involved in the regulation of V-ATPase assembly and activity.

Ten proteins have been identified as the components of the internal structure (Fig. I-3) (9, 16, 34). In the present study, I identified five proteins as the dimer components. Other five proteins are likely involved in other parts, for example, bell at the front part of internal structure (Fig. I-3B) and parts of the intact chain structure which were lost in the fractionation (Fig. I-11H).

Possible force transmission mechanisms for gliding. The involvement of an internal ATPase in the gliding mechanism is based on the following five observations from the analysis of the "gliding head" of *M. mobile* protrusions and of the isolated gliding machinery: (a) The affinity for ATP estimated by the saturation extent is comparable between the ATPase activity of the internal structure and the speed of the gliding head (9). (b) Substrate binding and gliding speed of the gliding head are inhibited by azide, as well as the ATPase activity of the internal structure (9). (c) The chain in the internal structure undergoes conformational changes based on ATP hydrolysis (9, 10). (d) Among the 21 proteins identified from the gliding head, only MMOB1660 and -1670 could be suggested for ATPase from the amino acid sequences alone (9, 34). (e) Fluorescent protein tagging of components of the internal structure significantly affects the substrate binding of cell and the gliding speed (16).

The structure elucidated in the present study allows me to discuss the gliding mechanism in more detail. Previously, structural changes linked to ATP hydrolysis were reported: (I) EM studies showed 2 nm contraction of dimer intervals in the isolated chains (9), and (II) HS-AFM studies showed movements of individual dimers in the cell 9 nm perpendicular to the chain long axis and 2 nm into the cell (10). Considering these observations, I propose two different working models for the force transmission mechanism in gliding (Fig. I-12). In the “contraction model” (Fig. I-12 i), the force generated by the hexameric ring shortens the chain. The resulting displacement of the projections from the dimer to the cell membrane drives the hook structure of Gli521 like a “lever.” Then, the leg moves with the catch, pull, and release of the SOs. In the “rotation model” (Fig. I-12 ii), the force generated by the hexameric ring rotates MMOB1630 in the same way as F₁-ATPase. This rotation is transmitted across the cell membrane to the Gli521. The hook structure converts rotational motion into linear motion of the leg, similar to a crank. Previous studies have reported that *M. mobile* exhibits unitary steps of approximately 70 nm in size at no load (38, 70). In our models, both the rotation and contraction displacements are expected to be a few nanometers. These displacements may be amplified by the large surface structure complex formed by the 100 nm long Gli349 and 120 nm long Gli521, which show dimensions comparable to the step size, acting as a large gear (33). This conjecture could explain how a single leg exerts a force of 1.5 pN, smaller than that of conventional motor proteins such as myosin, dynein, and kinesin.

Evolution of *M. mobile* gliding. A previous study suggested that Gli349 evolved from a static binding receptor to parasitize the host (27). Considering this, the evolutionary origin of *M. mobile* gliding can now be discussed. ATP synthase, which is abundant on the cell membrane, could have been accidentally associated with the binding receptor and turned into a primitive motility system, which may have provided random cell spreading. The system was then refined under survival pressure, because motility might be beneficial to infection and evading the hosts immune system. For dimerization and chain formation, PGK was then incorporated into the gliding machinery, because PGK was working in close proximity to ATP synthase.

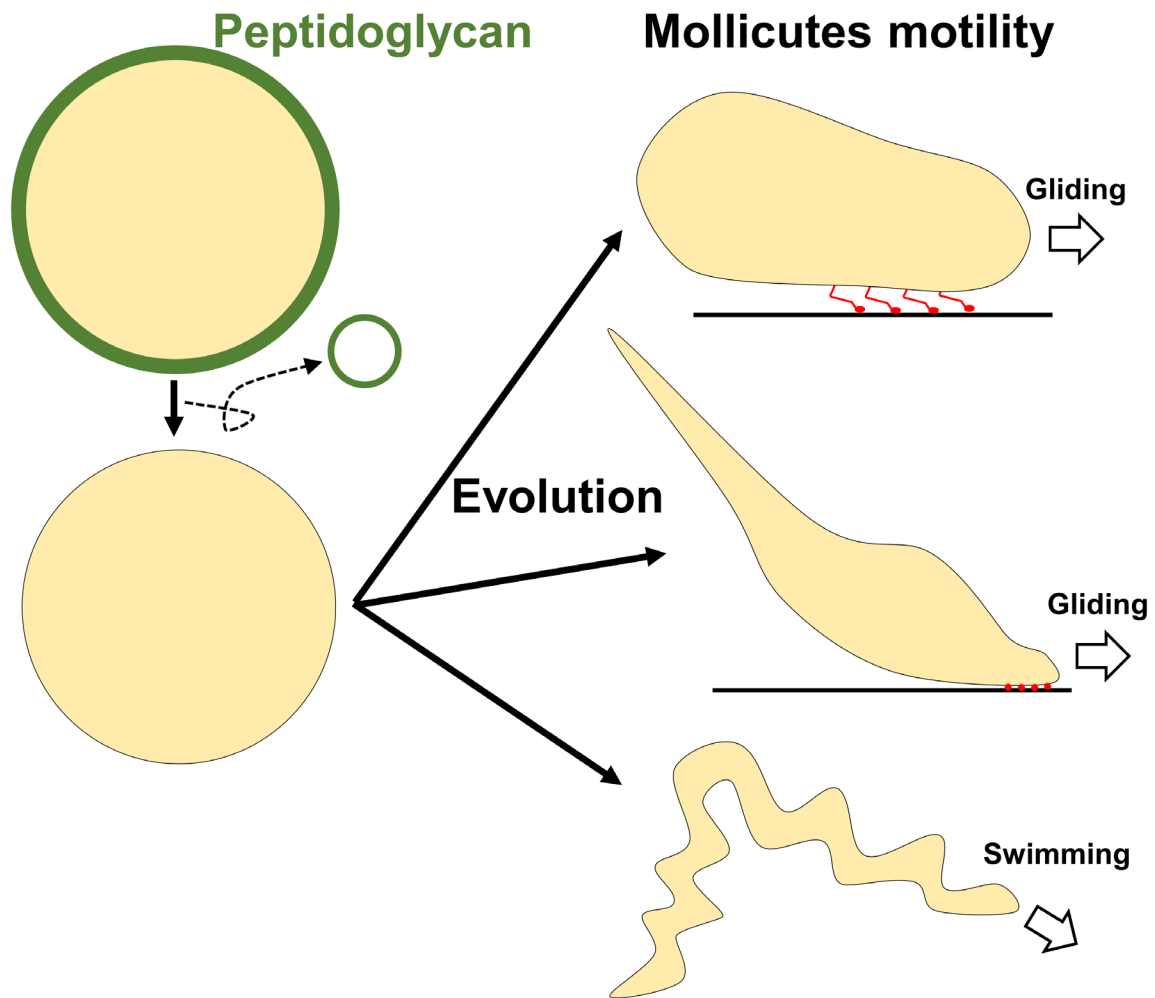


FIGURE I-1. Evolution model of Mollicutes motility. Mollicutes evolved three different types of motilities after losing genes related to peptidoglycan synthesis.

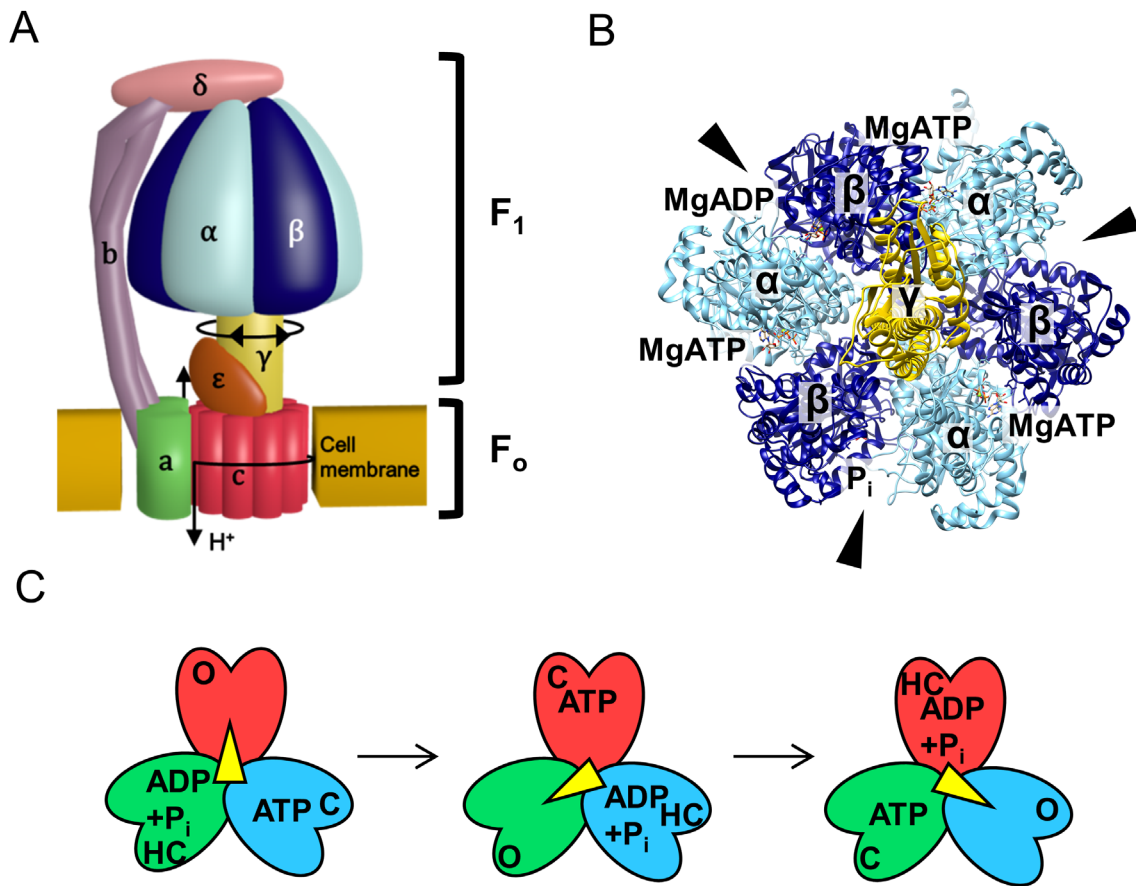


FIGURE I-2 Structure and mechanism of ATP synthase. (A) Illustration of bacterial ATP synthase. (B) Crystal structure of F₁-ATPase (PDB ID 6N2Y) (50). The structure was viewed from γ subunit in panel A. Three sites for ATP hydrolysis by triangles. (C) Schematic model of rotary catalytic mechanism. Illustrations are viewed from the same orientation as panel B. The catalytic site is located at each $\alpha\beta$ dimer. Three β subunits adopt different conformations: Closed (C), Half-closed (HC) and Open (O), respectively. The β subunit changes three conformations sequentially during ATP hydrolysis, resulting in counterclockwise rotation of central stalk.

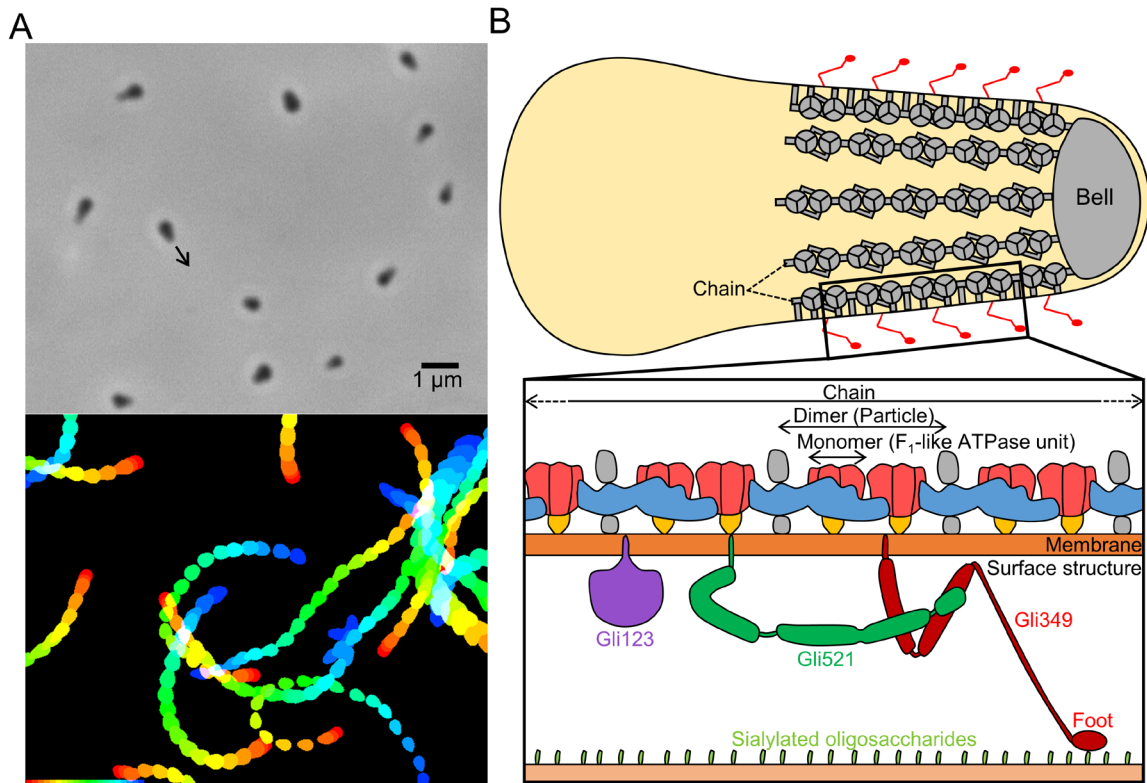


FIGURE I-3. *Mycoplasma mobile* gliding. (A) Optical microscopy of cells (upper) and trajectories of gliding cells (lower). All cells are gliding in the direction of tapered end as indicated by a black arrow. For trajectories, video frames of every 0.2 s were colored differently from red to blue and stacked for 4 s. (B) Schematic illustration of gliding machinery based on the Chapter I data. In the whole cell shown in upper illustration, the internal structure and legs are colored gray and red, respectively. The actual cell has about 28 chains, each consisting of 17 particles and connecting to bell, although a more limited number is illustrated here. In this paper I refer to particle and F_1 -like ATPase unit as the “dimer” and the “monomer,” respectively. A single unit of the surface structure and a chain of the internal structure are magnified in the lower illustration. (C) ORFs for the internal structure. The components of the internal structure are colored gray. Type 2 ATPase operon is at the top. Dimer components revealed in Chapter I are marked by colored boxes, corresponding to the colored components of the lower illustration in panel B.

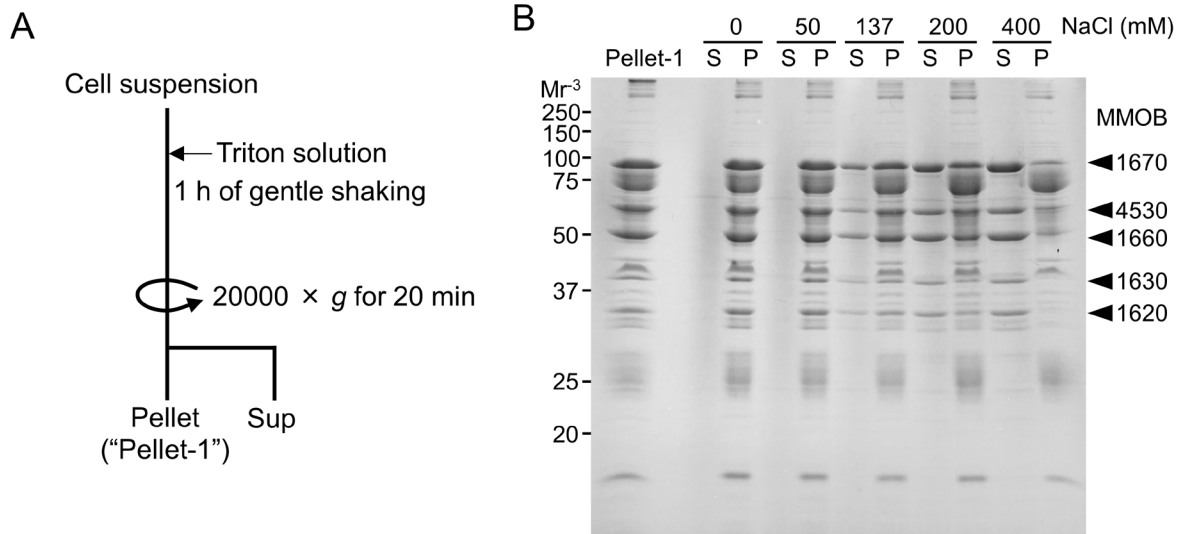


FIGURE I-4 Solubilization of chain components. (A) Fractionation procedure of pellet-1. Pellet from cell treated by Triton was named as “pellet-1.” Supernatant is abbreviated as “sup.” (B) Solubility of the chain components. Pellet-1 fraction was treated with buffers containing the specified concentrations of NaCl and centrifuged. Pellet-1 fraction, the supernatants (S) and the pellets (P) were analyzed by SDS-12.5% PAGE. See Materials and Methods for details.

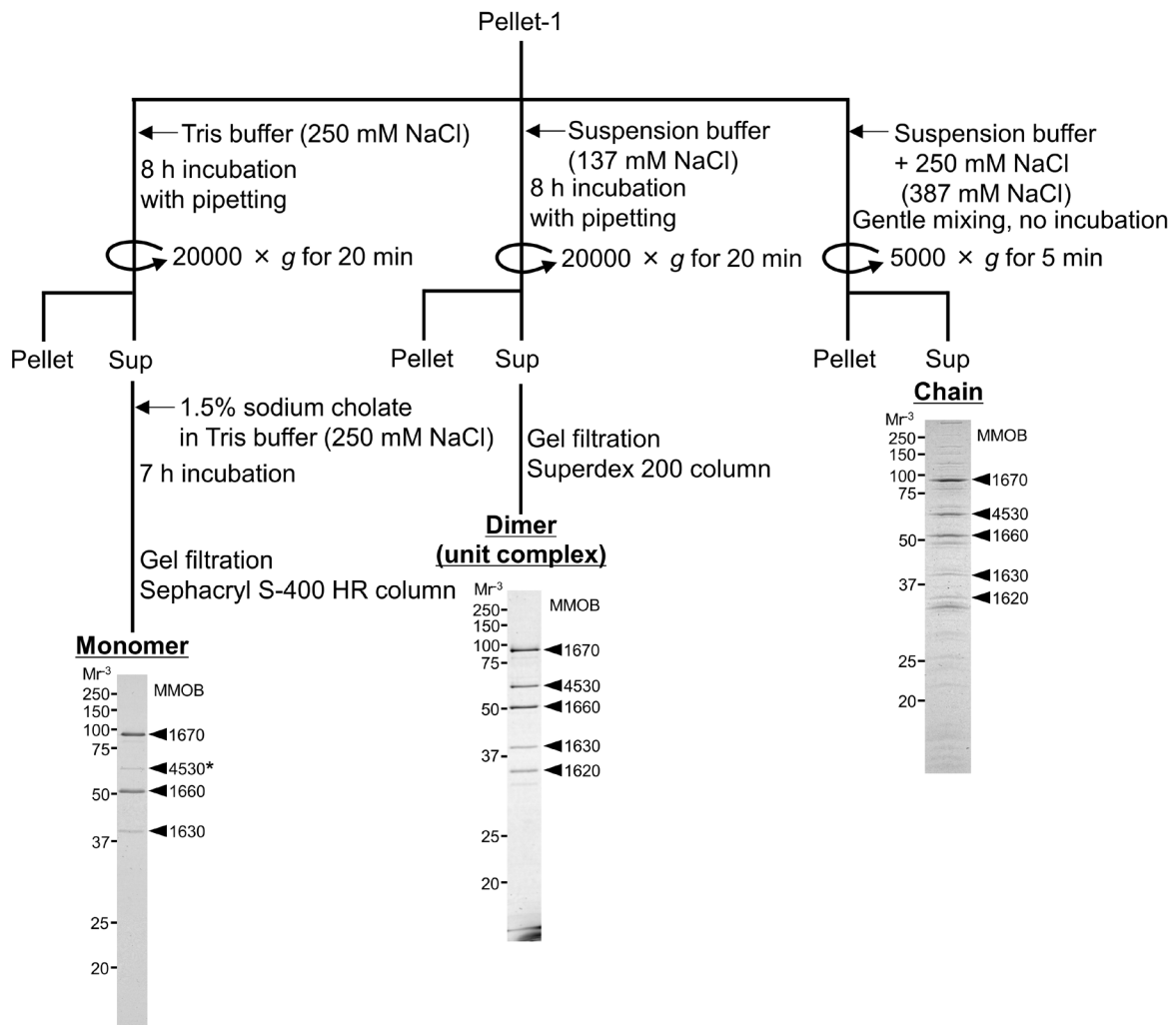


FIGURE I-5 Isolation procedure for three fractions. Each fraction was obtained from pellet-1 fraction. The adjusted concentrations of NaCl in the solution are indicated in parentheses. Supernatant is abbreviated as “sup.” Dimer (unit complex), monomer, and chain fractions were subjected to SDS-12.5% PAGE gel and stained with CBB. The bands marked by black triangles were identified by peptide mass fingerprinting (PMF). The intensity of band marked by an asterisk is reduced in monomer fraction. Molecular masses are shown on the left. See Materials and Methods for details.

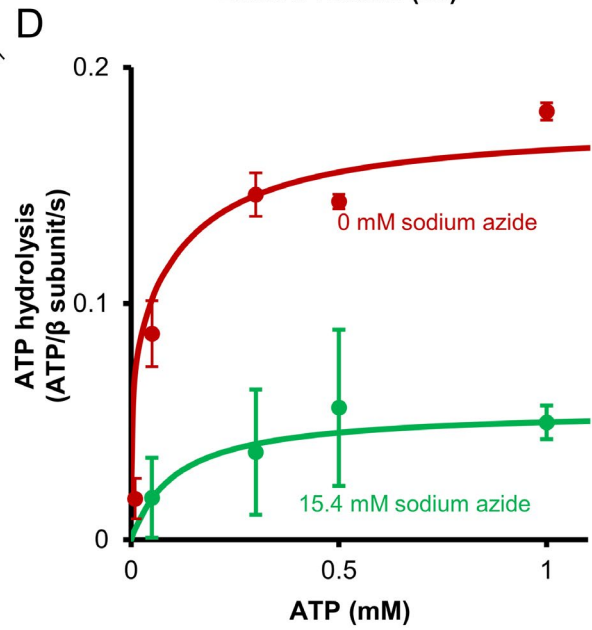
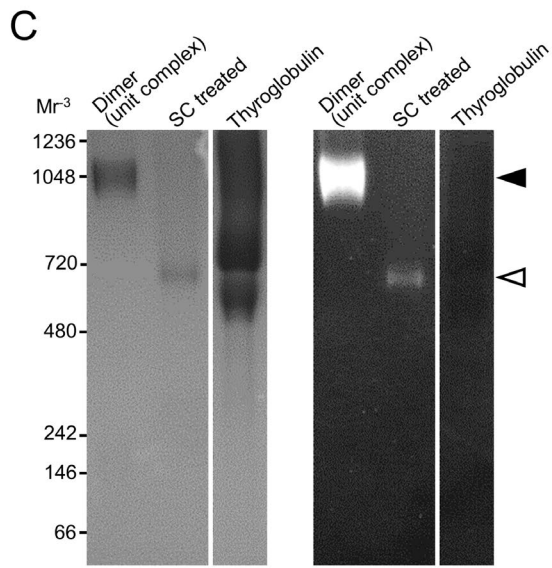
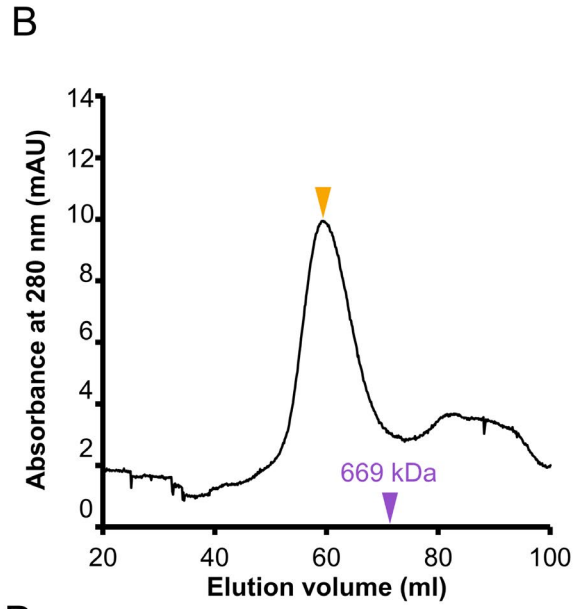
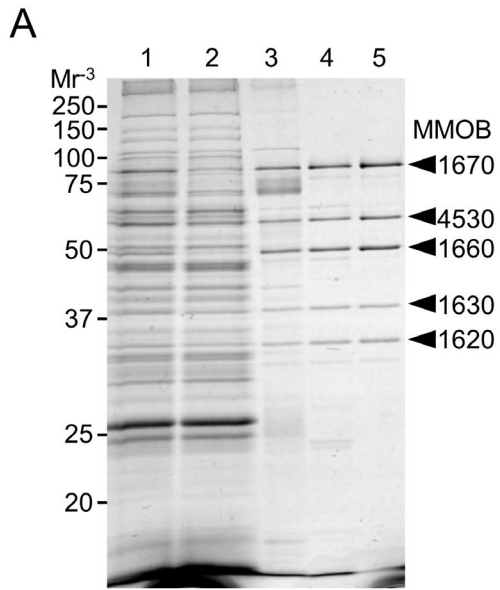


FIGURE I-6 Protein profile and characterization of dimer. (A) Isolation of dimer (unit complex). The fractions of each step were subjected to SDS-12.5% PAGE gel and stained with CBB. Lane 1, lysate of *M. mobile* cells; lane 2, Triton-soluble fraction; lane 3, Triton-insoluble (pellet-1) fraction; lane 4, supernatant after incubation in suspension buffer containing 137 mM NaCl; lane 5, peak fraction of Superdex 200 gel filtration chromatography. The bands of dimer components are marked by black triangles. (B) Gel filtration assay of unit complex fraction using Sephacryl S-400 HR column. The peak positions of unit complex (dimer) and thyroglobulin (669 kDa) are marked by orange and purple triangles. (C) BN-PAGE (left) and In-gel ATPase activity assay (right). dimer, dimer treated with 1.5% sodium cholate (SC treated), and thyroglobulin, which has no ATPase activity, were subjected to 3 to 12% gradient BN-PAGE. The bands of dimer and monomer after sodium cholate treatment are marked by closed and open triangles. White lead phosphate bands, indicating ATPase activity appeared in the right panel. Molecular masses are shown on the left. (D) Phosphate release assay of dimer under various ATP concentrations with and without sodium azide. The ATPase activities under 0- and 15.4-mM sodium azide are marked by red and green filled circles, respectively ($n = 3$). These data were fitted by the Michaelis-Menten equation as solid lines.

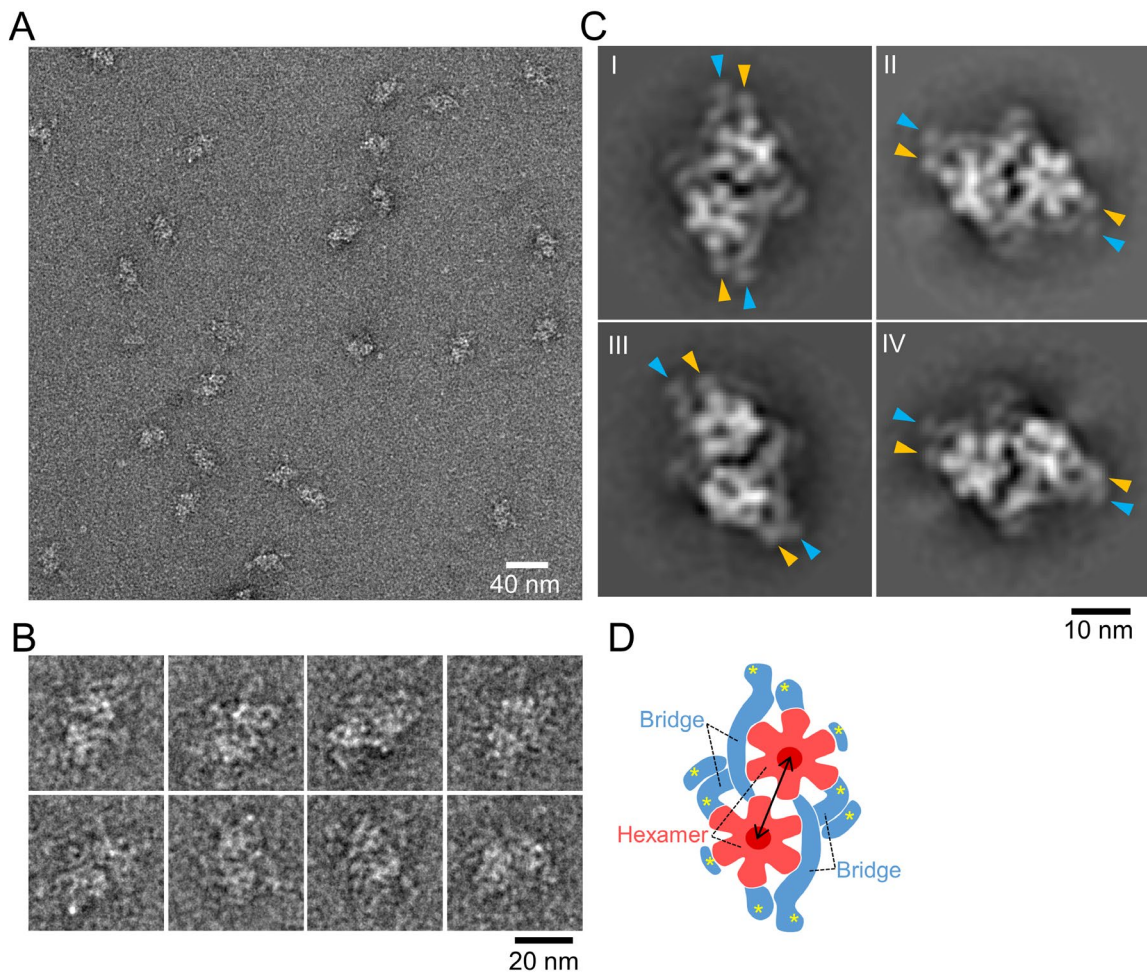


FIGURE I-7. Negative-staining EM of dimer. (A) Electron micrograph of negatively stained particles in unit complex fraction. (B) Images of individual particles. (C) Representative 2D averaged images. Mirror images are shown to match the orientation of the hexameric ring observed by HS-AFM in Fig. I-8. These images have common features as represented long and short protrusions marked by light blue and orange triangles, respectively. (D) Illustration based on the averaged image in left upper of panel C. Filamentous structures are marked by asterisks at an end. The double-headed arrow shows the distance between the centers of the hexamers.

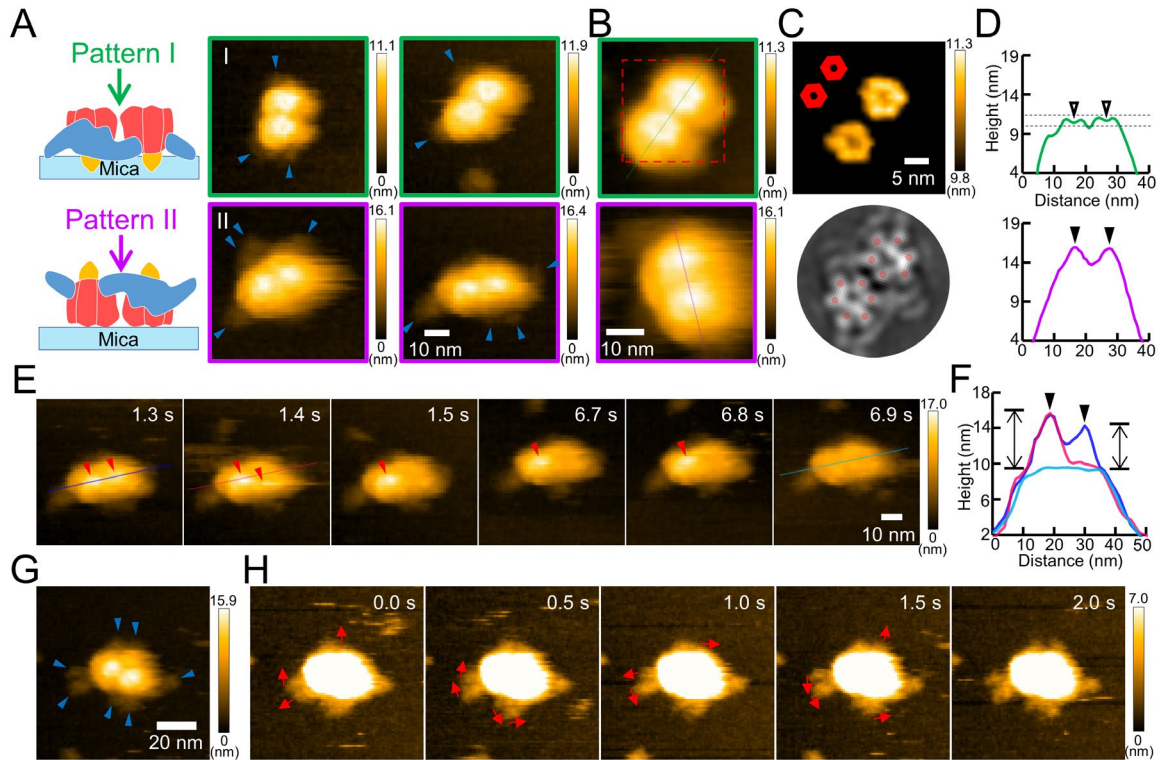


FIGURE I-8. HS-AFM of a dimer. (A) Two patterns of HS-AFM images. A dimer was scanned at 56×56 pixels in an area of $70 \times 70 \text{ nm}^2$ with a scanning rate of 100 ms per frame. Illustrations for patterns I and II (left side) were depicted based on 3D chain model shown in Fig. I-11. Observation directions are indicated by arrows. Lateral protrusions are marked by blue triangles. Images of patterns I and II are shown in green and purple frames, respectively. (B) Averaged images for patterns I (green frame) and II (purple frame). Dimer was scanned at 50×50 pixels in an area of $40 \times 40 \text{ nm}^2$ with a scanning rate of 100 ms per frame. The images were produced by averaging three successive video frames. (C) HS-AFM slice image showing two hexameric rings (upper) and averaged EM image (lower). Upper: The red broken boxed area in panel B was sliced for the height 9.8–11.3 nm from the substrate surface, processed for smoothing, and magnified. The angle alignments of two hexamers are schematically shown in the left upper. Lower: The central part of the left upper panel of Fig. I-7C was excised and aligned to compare with the upper panel. Subunits of the hexamer are marked by red circles. (D) Surface profiles along the lines in pattern I (green) and II (purple). The upper and lower images in panel B were each profiled at the green and purple lines passing the globule centers. The dimples and the peaks are marked by open and black triangles, respectively. The slice height in panel C is shown by broken lines. (E) Shedding process of the peaks of pattern II particle shown in panel A. The peaks are marked by red triangles. (F) Surface profile showing the disappeared peaks. The images in panel E were each profiled at the blue, pink, and light blue lines passing the globule centers. The peaks are marked by black triangles. The double-headed arrows show the peak heights. (G) HS-AFM image of a dimer with seven lateral protrusions. Dimer was scanned at 120×120 pixels in an area of $120 \times 120 \text{ nm}^2$ with a scanning rate of 500 ms per frame. Lateral protrusions are indicated by blue triangles. (H) Fluctuations of the protrusions of the particle shown in panel G. The images were sliced for the height 0–7.0 nm from the substrate surface. The moving directions are indicated by arrows. In all HS-AFM images, the color bar on the right shows the range of image heights.

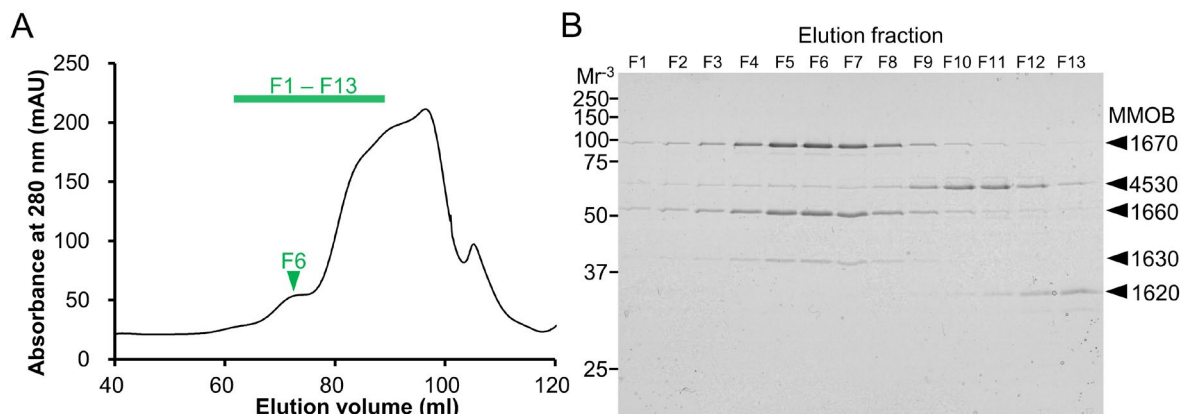


FIGURE I-9 Monomer isolation. (A) Gel filtration profile in monomer isolation using a Sephacryl S-400 HR column. The small peak is marked by a green triangle. (B) The F1–F13 fractions in the gel filtration indicated by the green line in panel A were subjected to SDS-12.5% PAGE and stained with CBB. F6, which corresponds to the small peak in the gel filtration, was used for further analyses as monomer fraction. Bands of dimer components are marked by black triangles. Focused proteins were identified by PMF, and molecular masses are shown on the left.

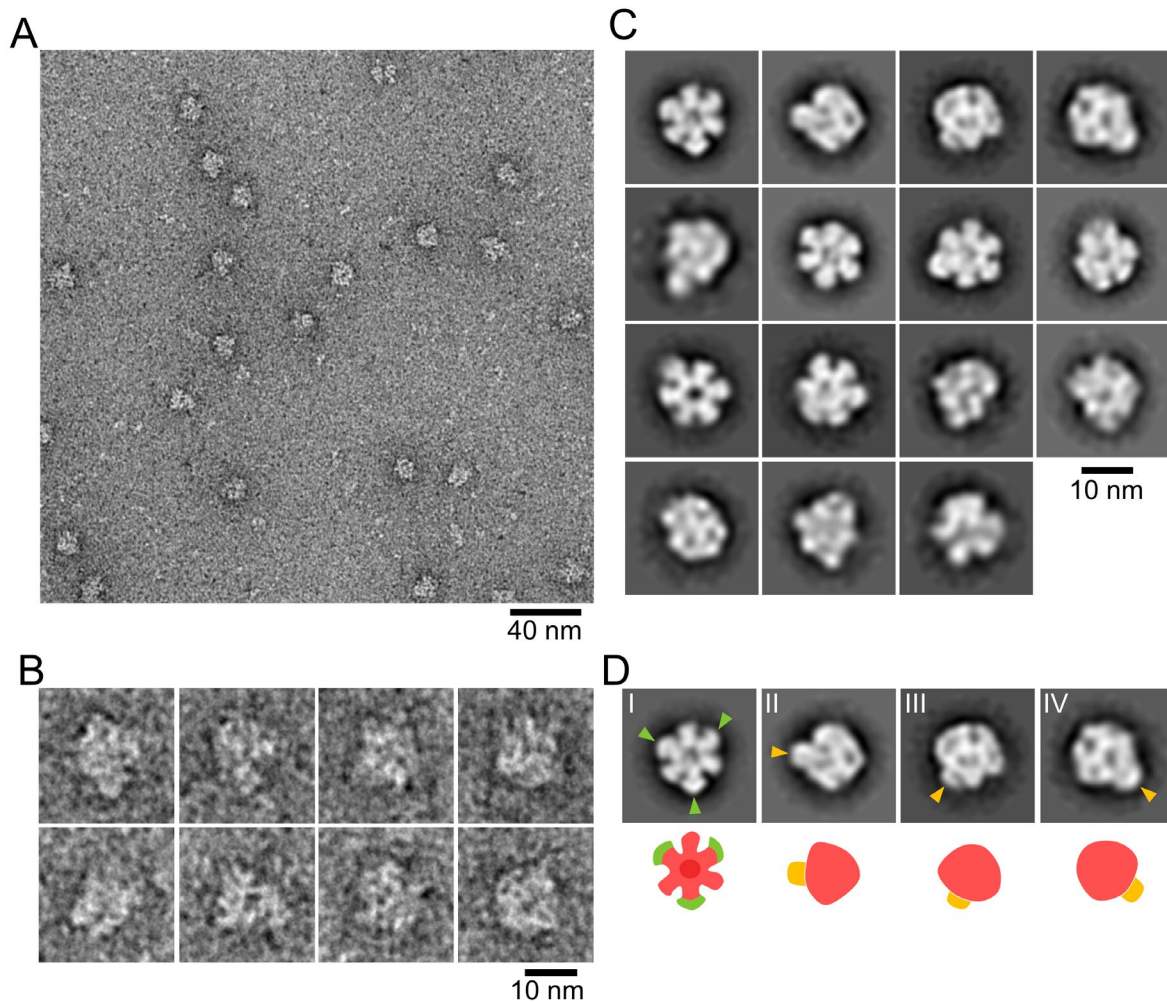


FIGURE I-10. Negative-staining EM of monomer fraction. (A) Electron micrograph of negatively stained ATPase in monomer fraction. (B) Images of individual particles. (C) Representative 2D averaged images. (D) Selected 2D averaged images (upper) and depictions of their structures (lower). Upper: Hook structures in the hexameric ring and the stalks are marked by green and orange triangles, respectively. Lower: The hexameric part, hook structures and the stalk are colored rose, green and orange, respectively.

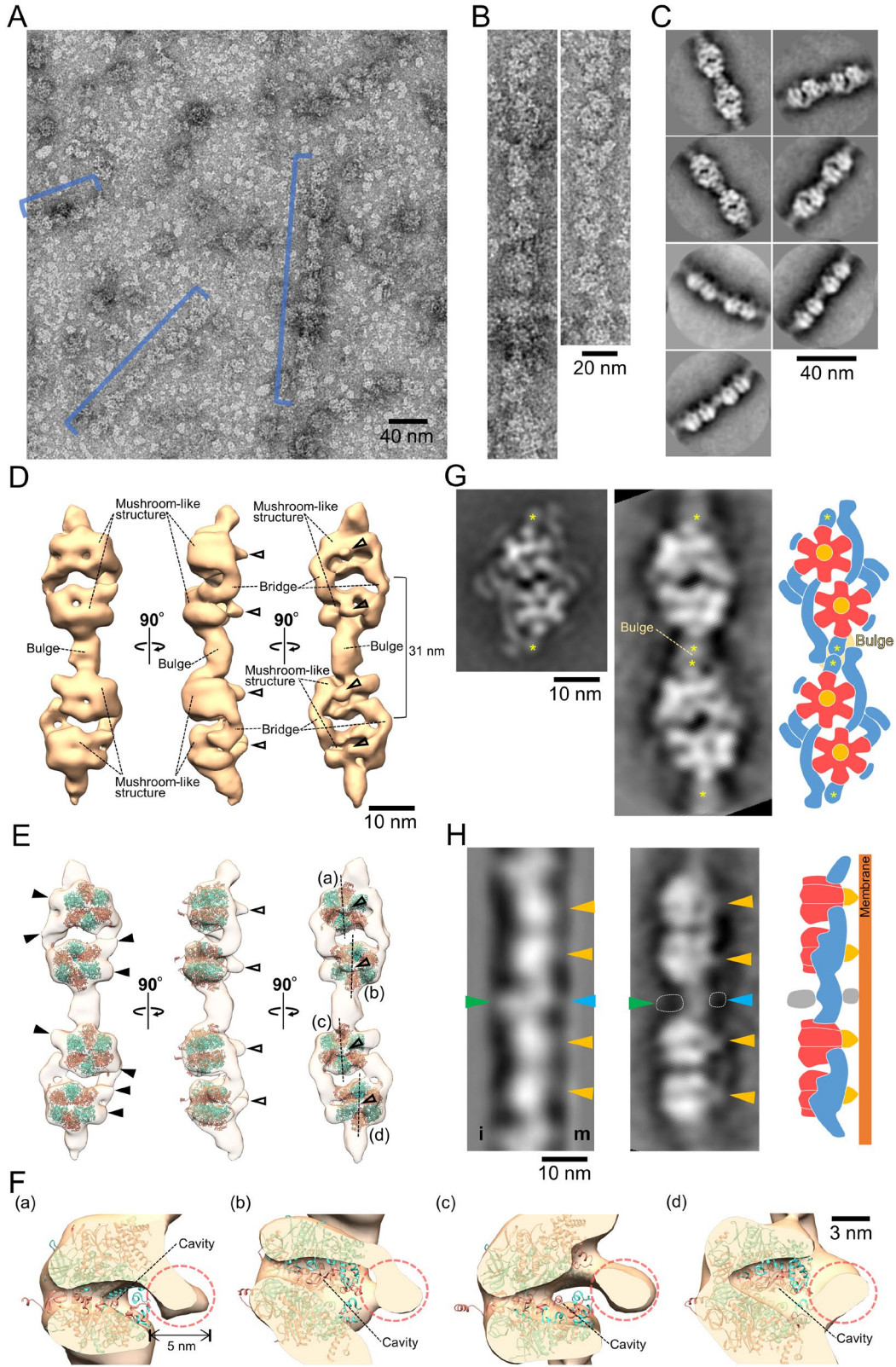


FIGURE I-11. Chain structure. (A) Electron micrograph of a negatively stained chain. The chain structures are marked by blue lines. (B) Magnified chain images. (C) Representative 2D averaged images. (D) Three-dimensional reconstruction of a chain containing two F_1 -like ATPase dimers. The 3D map is visualized at a density threshold (contour level = 0.026). The central stalks are marked by open triangles. (E) Superposition of the atomic model of *Bacillus* F_1 -ATPase catalytic $(\alpha\beta)_3$ (PDB ID 6N2Y) (50) onto the 3D chain structure. The α and β subunits are colored salmon and turquoise, respectively. The central stalk and protrusions from hexameric rings are marked by open and black triangles, respectively. (F) Cross section of mushroom-like structures. Central stalks are marked by broken circles. The double-headed arrow shows the length of the protrusion. Corresponding mushroom-like structures are marked (a) to (d) in panel E. (G) Comparison between the dimer image from Fig. I-7C (left) and the chain reprojection (middle). The reprojected image is viewed from the angle used for the right image of panel D. Short filaments corresponding to the position of the connecting bulge are marked by asterisks. A depiction of a chain model based on the comparison (right). (H) Comparison between the averaged chain image from ECT (left) and the chain reprojection (middle). Left: The averaged chain image was modified from the whole cell ECT image in the previous study (9). Inner sides and membrane sides relative to the chain are marked by i and m, respectively. Middle: Chain was reprojected from an angle close to the middle image in panel D. The protrusion from the globule corresponding to the central stalk from the hexameric ring, one from the connecting bulge and the globule attached to the connecting bulge are marked by orange, light blue and green triangles, respectively. The areas of image densities that were visualized only in the ECT image are marked by broken lines. Right: An illustration depicts a chain model based on the comparison.

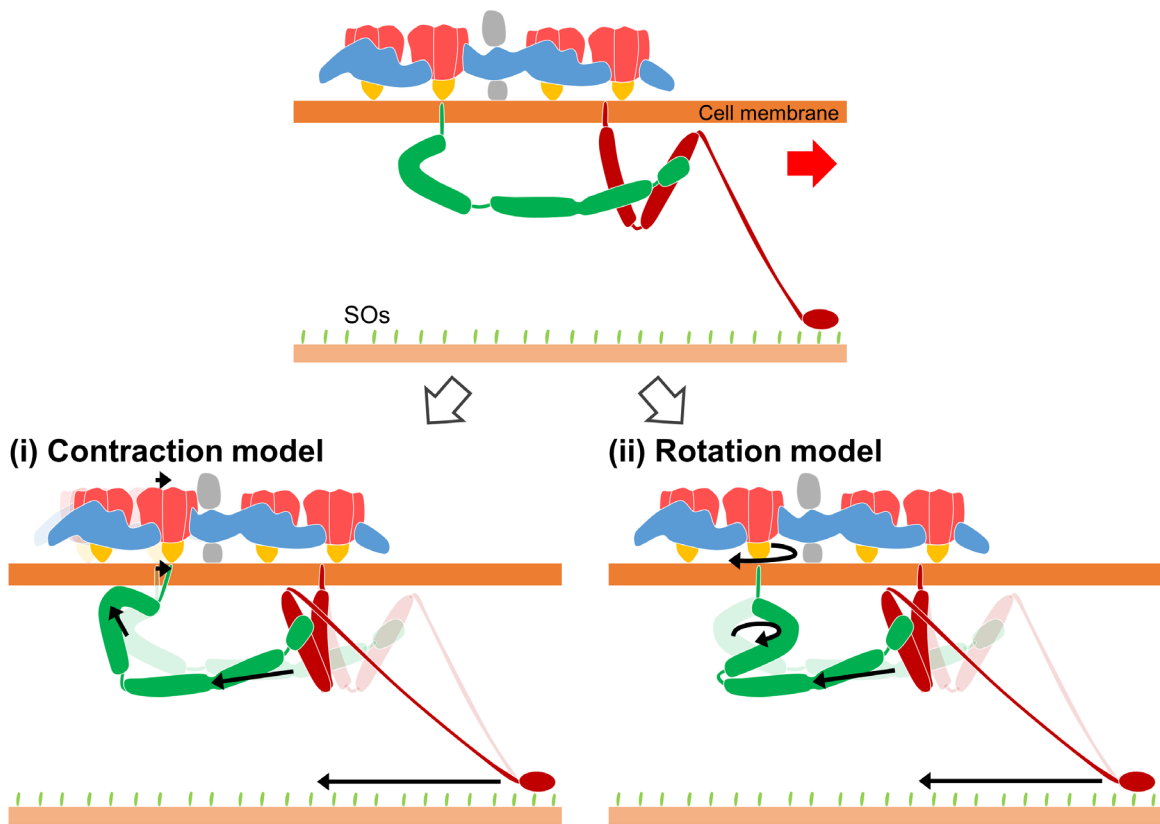


FIGURE I-12. Working models for force transmission mechanism. The gliding direction is indicated by a red arrow. The regions marked in gray were visualized only in the ECT image. The crank protein Gli521 and the leg protein Gli349 are colored green and red, respectively. (i) Contraction model: The force generated by the hexameric ring displaces the dimer along the gliding direction. The displacements are transmitted through the membrane to Gli521. (ii) Rotation model: The force generated by the hexameric ring rotates the central stalk in a mechanism similar to that of F_1 -ATPase. The rotational motion is transmitted across the membrane to Gli521. The generation and transmission of forces are presented by black arrows for both models.

CHAPTER II

CryoEM structure of dimeric F₁-like ATPase in *Mycoplasma mobile* gliding machinery

ABSTRACT

Mycoplasma mobile glides on solid surfaces with a unique mechanism. The gliding force is generated by an internal motor and transmitted to the surface leg structure. I reported the structure of the motor as “dimer” unit in Chapter I, but much higher resolution was required to clarify the force generation mechanism. I obtained the 3D structure of Dimer at 5.7 Å resolution by electron cryomicroscopy. Atomic models predicted by sequence homology were fitted to the 3D map. Two $\alpha_3\beta_3$ hexamers with a central shaft in each of them form a paired structure with a rectangular frame. The motor is featured by six arms, each composed of phosphoglycerate kinase (PGK), protruding from the β subunit homolog of ATP synthase. The three β subunit homologs show different conformations in each hexamer, suggesting a rotational catalytic mechanism analogous to ATP synthase. Three α subunit homologs also show different conformations, which may cause motor-chain retraction discussed previously. In this study, I propose possible force generation processes in the gliding mechanism.

INTRODUCTION

The structure of the motor for *M. mobile* gliding was revealed by negative-staining EM in Chapter I. The high-resolution structure should provide information on subunit composition, residue positions, and transition states during the enzymatic reaction, allowing for a more detailed discussion of the force generation mechanism.

Electron cryomicroscopy (cryoEM) is a powerful tool which can visualize biomolecules in a frozen hydrated state (71). The resolution of cryoEM has reached up to approximately 1.25 Å, while the resolution of negative-staining EM is limited to a maximum of approximately 18 Å (72, 73). In cryoEM method, the sample is flash frozen in liquid ethane at approximately -160 °C. The flash freezing of water into vitreous ice protects the specimen from drying out and radiation damage in transmission electron microscopy (TEM). The sample in vitreous ice is then observed by using TEM incorporating liquid-nitrogen cooled sample stage.

In this study, I applied cryoEM to “dimer” unit of *M. mobile* motor and determined the 3D structure at 5.7 Å resolution. Based on the constructed atomic model, I discuss the force generation mechanism of the motor.

MATERIALS AND METHODS

CryoEM and image processing. Isolation of the dimer was done by the same procedure as in Chapter I. The 2.6 μ L of the dimer solution was placed on a glow-discharged grid. The grid was then automatically blotted from both sides with filter

paper at 25 °C for 8 s and vitrified using a semi-automated vitrification device (Vitrobot; FEI, Eindhoven, Netherlands). The images were observed and captured at 1.07 Å/pixel by a Titan Krios FEG transmission electron microscope (FEI) operated at 300 kV on an FEI Falcon II 4 k × 4 k direct electron detector (FEI).

The contrast transfer function parameters for electron micrographs were estimated using Gctf. Further image processing was performed using RELION 3.0. A total of 101746 particles was automatically selected with box sizes of 432 × 432 pixels using reference-based auto-picking. These particle images were binned to 4.28 Å/pixel. The particle images were subjected to 2D classification. The selected 47738 particles were used to reconstruct the initial model with a final resolution limit of 15 Å. The initial model and selected 86093 particles were used to perform 3D classification. The resulting 2 classes were assessed manually and the class1 3D model with 46432 particles was used for further analyses. The particles were re-extracted with the pixel size returned to 2.14 Å/pixel. I performed 3D refinement to the dataset and yielded a 3D map with 8.1 Å resolution. CTF refinement and Bayesian polishing improved the resolution to 5.7 Å (74).

Structure modeling and refinement. I performed comparative modeling through the Robetta server (<https://robetta.bakerlab.org/>) (75) to generate homology models for Gliaβγ and PGK. Templates for homology models were F₁-ATPase α subunit from *Bacillus subtilis* (PDB ID 2QE7) (76), F₁-ATPase β subunit from *Saccharomyces cerevisiae* (PDB ID 3FKS) (77), F₁-ATPase γ subunit from *Paracoccus denitrificans* (PDB ID 5DN6) (78) and PGK from *Thermus caldophilus*

(PDB ID 2IE8) (79). The generated structures were fitted to the corresponding densities in the cryoEM map by Situs program (80). These fitting were then improved with molecular dynamics flexible fitting (81). Their fitted models were manually inspected and adjusted by using COOT (82) and refined several times by using phenix.real_space_refine (83). The segmentation of 3D maps was performed with UCSF Chimera.

RESULTS

CryoEM of a dimer. I performed cryoEM on a dimer (Fig. II-1). I picked 101746 particle images automatically using RELION software for 2D-classification (Fig. II-1A and B). From the 2D-classification, I obtained clear particle images (Fig. II-1C). A set of 46432 particle images was selected through the 2D-classification and used to reconstruct a 3D structure at 5.7 Å resolution with C1 symmetry. The analysis workflow is summarized in Fig. II-2.

Overall structure of a dimer. The cryoEM structure showed a supramolecular complex with a size of 50 × 35 × 20 nm and consisting of more than 20 subunits with an estimated total of 1.5 MDa (Fig. II-3A–C). Consistent with the results of Chapter I, two mushroom structures of 15 nm size, reminiscent of F₁-ATPase, consisting of a characteristic hexameric ring and a central stalk, formed a pair almost in two-fold symmetry. The hexameric ring was composed of alternating subunits each similar to the α and β subunits of F₁-ATPase. The central stalk

piercing the hexameric ring showed two clear α -helices seen through the cross-section of the hexameric ring as γ subunit in F_1 -ATPase (Fig. II-3D). The two α -helices were connected to a 5 nm diameter globular domain protruding from the hexameric ring (Fig. II-3B).

The two hexamers were cross-linked by two $7 \times 3 \times 3$ nm rod-like "bridges" bound to the α -like subunit (Fig. II-3C). Across the bridges, two α -helix structures were attached to the α -like subunits. These two α -helix structures are reminiscent of the buttress structure that connects the AAA+ ring and stalk in dynein (84). The paired hexameric rings had two radially protruding 3 nm-long arm structures (short arm1 and -2) and six 10 nm-long arm structures (long arm1 to -6) (Fig. II-3A). Long arms consisted of two globular domains of approximately 5 nm diameter, while short arms consisted of a single globular domain of approximately 4 nm diameter. Long arm3 and -6 and the domain at the tip of long arm1 were only visualized below a density threshold (contour level = 0.03) due to the flexibility of the structures.

Next, to identify the proteins in each subunit, I generated homology models for MMOBs 1660 (1–528aa), 1670 (300–772aa), 1630 (1–336aa) and 4530 (1–397aa) using the structures of ATP synthase subunits and PGK from different bacteria as templates. The four generated models were then fitted to the EM map by rigid body fitting and subsequent molecular dynamics flexible fitting (Fig. II-4E–G). The 1–528 aa region of the α -homolog encoded by MMOB1660 was fitted to α -like subunits in the heterohexameric ring, while the 300–772 aa region of the β -homolog encoded

by MMOB1670 was fitted to β -like subunits. I named α - and β -like subunits Gli α and Gli β , respectively. All Gli β has an extra structure consisting of a linker and a bulge structure (Fig. II-5B–D). The extra structure should correspond to the extra N-terminal region of MMOB1670 (1–299aa). The details are to be mentioned later. At the hexamer interface, Gli β_1 and Gli β_4 interacted between loops 382–433aa (Fig. II-3H). In the hexameric ring, five of the six Gli $\alpha\beta$ interfaces had small molecule densities but could not be identified due to resolution limitations (Fig. II-4). These were thought to be phosphate and/or cell-derived nucleotides, as the samples were isolated and observed in a buffer containing 9.6 mM phosphate. The 1–329aa region of the protein encoded by MMOB1630 was fitted to the central stalk. I named this γ -like subunit Gli γ (Fig. II-3E–G). The widely conserved 1–397aa region of PGK (511aa) was fitted to each long arm 1 to -6. The fitting of 1–192 aa and 383–397aa to the tip domain of long arm 1 and 1–397aa to long arm 3 and -6, respectively, was done only by rigid body fitting using the Situs program due to low resolution. The densities corresponding to the C-terminal region of 398–511aa, which is specific for PGK in *M. mobile*, were not visualized in all PGK arms. The short arms were all bound to Gli α and the two formed the bridge at the interface of the two hexamers (Fig. II-3I and J). I named these short arms GliD. GliD protein is thought to be encoded by MMOB1620, which is the only one of the dimer components not assigned to the cryoEM structure. Assuming that GliD is a sphere with a diameter of 4 nm and that the protein mass is 1.37 g/cm³ (85), its molecular weight is about 27.6 kDa, which is slightly smaller than the estimated molecular

weight 33.7 kDa of MMOB1620. There is an unassigned density surrounded by $\text{Gli}\alpha_1$ and the bulge structures of $\text{Gli}\beta_2$ and $\text{Gli}\beta_4$ (Fig. II-3K). The density may be the structure of $\text{Gli}\beta$, extending from the bulge structure.

Subunit structures. $\text{Gli}\alpha_{1-3}\beta_{1-3}\gamma_1$ and its counterpart $\text{Gli}\alpha_{4-6}\beta_{4-6}\gamma_2$ showed no structural differences at the present resolution except for the $\text{Gli}\beta$ N-terminal domain. $\text{Gli}\alpha$ and $\text{Gli}\beta$ had three domains conserved in the F_1 -ATPase subunits α/β : a crown domain consisting of six β -strands, an ATPase domain with a nucleotide-binding site, and a C-terminal domain consisting of a bundle of α -helices (Fig. II-5A–D). Walker A motif, GGAGVGKT, that binds to the phosphate group of nucleotides, was found in the ATPase domains of both $\text{Gli}\alpha$ and $\text{Gli}\beta$. β -subunits of all F_1 -ATPases found so far have a loop between two long α -helices in the C-terminal domain, and it is commonly called the DELSEED loop because it is formed by residue DELSEED (14). $\text{Gli}\beta$ had a loop with the similar sequence DALSEDD (residues 684–690) in an equivalent position to the DELSEED loop of F_1 -ATPase (Fig. II-5B). Hereafter I refer the DALSEDD loop as to DELSEED loop. The atomic models of $\text{Gli}\alpha_3$ (1–528aa) and $\text{Gli}\beta_1$ (300–772aa) are superimposed on the corresponding parts of the *Bacillus* F_1 -ATPase (PDB ID 6N2Y) (50), α (2–501aa) and β (2–471aa), respectively, showing structural similarity (Fig. II-5E and F).

$\text{Gli}\alpha$ does not have an α -helix corresponding to the N-terminal α -helix (H1) of the α -subunit of F_1 -ATPase (2–17aa), which is the binding region for the peripheral stalk (Fig. II-5E). This observation is consistent with the fact that there is no homologue of the gene that constitutes the peripheral stalk on the Type 2 ATPase

operon. The 501–528aa of Gli α is part of the C-terminal region that is non-homologous to the α -subunit of F₁-ATPase and formed two α -helices, helix14 (H14) and helix15 (H15). A striking difference between Gli β and the F₁-ATPase β subunit is the presence of the linker and the bulge consisting of an extra N-terminal region (1–299aa) (Fig. II-5B–D). The linker and bulge of all six Gli β subunits extend from the crown domain, and they show slightly different aspects and can be divided into three types based on their structural features: Type A of Gli β _{1,4}, Type B of Gli β _{2,5}, and Type C of Gli β _{3,6} (Fig. II-5B–D, II-6). Gli γ was composed of two long α -helices at the N- and C-termini and a globular domain composed of β -sheets and surrounding α -helices (Fig. II-5G). The superposition of Gli γ (1–329aa) with the γ subunit (2–284aa) of *Bacillus* F₁-ATPase (PDB ID 6N2Y) showed a structural similarity (Fig. II-5H). The N-terminal α -helix of Gli γ was more straightforward with respect to the C-terminal α -helix compared to that of the γ -subunit of F₁-ATPase. The C-terminal α -helix was approximately 3 nm longer than that of the γ -subunit of the F₁-ATPase. PGK structure solved in this study is composed of two domains connected by hinge structure (Fig. II-5I), which is identical to that of conventional PGK (79). The C-terminal domain (CTD) of all PGK was in contact only with each of the three types of Gli β bulge (Fig. II-5J–L).

Structural differences in hexamer. To investigate the conformational differences in Gli $\alpha\beta$, I superimposed Gli β ₁₋₃ and Gli α ₁₋₃, respectively (Fig. II-7A and B). Gli β showed a large structural difference in the C-terminal domain (Fig. II-7A). Gli β ₃ adopts a closed conformation (C) with the ATPase domain as a lever and the

C-terminal domain swinging to the Gli_γ side. $\text{Gli}\beta_2$ adopts a half-closed conformation (HC) with a slight swing at the C-terminus, and $\text{Gli}\beta_1$ adopts an open conformation (O). I found a large structural difference between the three non-catalytic subunits of $\text{Gli}\alpha$ in helix 12 (H12) to helix 15 (H15), which are composed of 448-519 aa specific for Type 2-ATPase (Fig. II-7B and C). The H12 of $\text{Gli}\alpha_3$ was shifted up to approximately 0.5 nm toward Gli_γ relative to the other two (Fig. II-7C). Furthermore, the ring-like structure formed by H13–H15 of $\text{Gli}\alpha_3$ was shifted by approximately 1 nm toward Gli_γ relative to the other two. H12–H15 of $\text{Gli}\alpha_2$ was slightly shifted from that of $\text{Gli}\alpha_1$ toward Gli_γ . I defined the conformations of $\text{Gli}\alpha_{1-3}$ as "Open" (O), "Half-Closed" (HC), and "Closed" (C), as well as the β -subunits. The two hexamer rings formed an asymmetrical structure, with $\alpha_0\beta_0$, $\alpha_C\beta_C$, and $\alpha_{\text{HC}}\beta_{\text{HC}}$ dimers arranged in a clockwise direction when viewed from the C-terminus (Fig. II-6D). Only the catalytic site of $\text{Gli}\alpha_0\beta_0$ ($\alpha_1\beta_1$) dimer did not bind the small molecule density (Fig. II-4, left upper). The conformational arrangement with substrate binding in the hexamer is parallel to that of the β -subunit in F_1 -ATPase.

Next, I focus on the catalytic site at the $\text{Gli}\alpha\beta$ dimer interface (Fig. II-7E). Superposition of the catalytic site of $\text{Gli}\alpha_C\beta_C$ dimer into that of bovine F_1 -ATPase $\alpha\beta$ dimer revealed that three essential residues in the catalytic reaction of F_1 -ATPase, $\beta/\text{K458}$ (P-loop lysine), $\beta/\text{E484}$ (catalytic residue), and $\alpha/\text{R344}$ (arginine finger), are conserved (14).

These results suggest that the dimer is driven by a rotary catalytic mechanism in which three catalytic subunits continuously hydrolyze ATP in the same direction

as the F₁-ATPase. In F₁-ATPase, the force generated by the conformational change of the β -subunit is suggested to be mainly transmitted through the interaction between the DELSEED loop and the globular domain of γ -subunit (14). I focus on the interaction between the C-terminal domains of Gli $\alpha\beta$ and the globular domain of Gli γ . The DELSEED loop of Gli β_1 (Open) interacted with the globular domain of Gli γ (Fig. II-7F). Furthermore, the H13–H15 ring structure in Gli α_3 (Closed) also interacted with the globular domain of Gli γ . Next, to investigate how the conformational change of Gli $\alpha\beta$ acts in the motor, I placed Gli $\beta_{2,3}$ and Gli $\alpha_{1,2}$ at the positions of Gli β_1 and Gli α_3 , respectively, in the dimer cryoEM map (Fig. II-7G). This placement showed that the C-terminal domain of β subunit shifted to push Gli γ by Open to Closed movement, and almost returns to the Open position by Closed to Half-closed movement. H12–H15 of Gli α shifted up to approximately 1 nm toward the interacting bridge (GliD) by Closed to Half-closed movements, and almost stayed at the position by Half-closed to Open movements. These results suggest that the three Gli β s rotate Gli γ by a rotary catalytic mechanism, and that the Gli α -specific C-terminal domain pushes the bridge (GliD) with a conformational change of approximately 1 nm.

Dimer connection for chain form. To investigate how the dimer structure obtained by cryoEM are connected, I compared the dimer structure with the chain 3D map obtained by negative-staining EM in Chapter I (Fig. II-8A, upper). The atomic models of Gli $\alpha_{1-6}\beta_{1-6}\gamma_{1,2}$ solved by cryoEM were fitted to the dimeric F₁-like ATPases in the chain 3D map (Fig. II-8A, middle). According to the fitting models, I

aligned the dimer cryoEM map to produce the montage image (Fig. II-8A, lower). The GliDs from the two dimers were oriented toward each other in the chain density map, suggesting that dimers are bound to each other through GliD (Fig. II-8B and C). Furthermore, the PGKs at the dimer interface were facing each other, although they have no corresponding density in the chain map. These possible interactions may also be involved in the dimer connection.

DISCUSSION

Rotary catalytic mechanism of dimer. The two F_1 -like ATPases in the dimer interacted through the C-terminal region of $Gli\alpha$, where the structural change is likely to occur. The structural changes may affect the neighboring monomer ATPase and give rise to cooperativity between monomers that is not present in the ATP synthase dimer in the catalytic reaction. Assuming cooperativity, I proposed a three-step reaction model for the dimer (Fig. II-9A).

The $Gli\alpha_0\beta_0$ dimer binds ATP and transitions to the $Gli\alpha_C\beta_C$ dimer because only $Gli\alpha_0\beta_0$ dimer have no density for small molecule at the catalytic site. When ATP is hydrolyzed and ADP and P_i are released, the $Gli\alpha_C\beta_C$ dimer transitions to the $Gli\alpha_{HC}\beta_{HC}$ dimer and then back to the $Gli\alpha_0\beta_0$ dimer. By analogy to the rotary catalytic mechanism of ATP synthase, the reactions in the hexamer are interlocked, with the three $Gli\beta$ s kicking $Gli\gamma$ in turn, making one rotation in three steps. In this reaction, a part of the C-terminal domain of $Gli\alpha$ contracts about 1 nm during the transition from O to C and extends about 1 nm during the transition from C to HC.

This sequence of conformational changes is probably caused by the rotational action of Gli γ through the interaction because the C-terminal domain of Gli α does not contact with the C-terminal domain of Gli β , which undergoes a conformational change. The conformational change of Gli α is thought to distort the bridge structure by pushing or pulling GliD, resulting in cooperativity in the catalytic reaction of the two hexamers. GliDs connecting chains at the dimer interface are also expected to be pushed and pulled by Gli α . The possible movement in GliDs causes the chain stretching discussed as contraction model in Chapter I (Fig. I-12i, II-9B). The change in distance is estimated to be 2 nm by adding the two 1 nm Gli α motion, which is consistent with the distance of contraction observed by previous EM study (9).

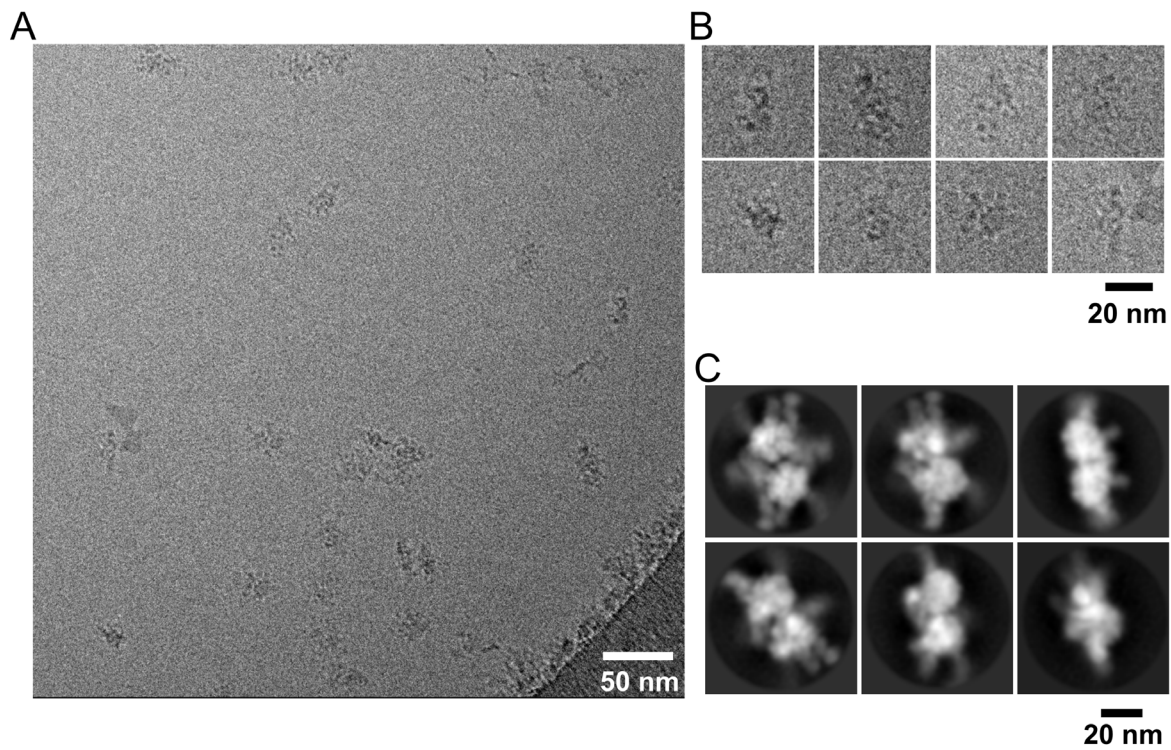


FIGURE II-1. CryoEM of a dimer. (A) Electron micrograph of a dimer. (B) Images of individual particles. (C) Representative 2D averaged images.

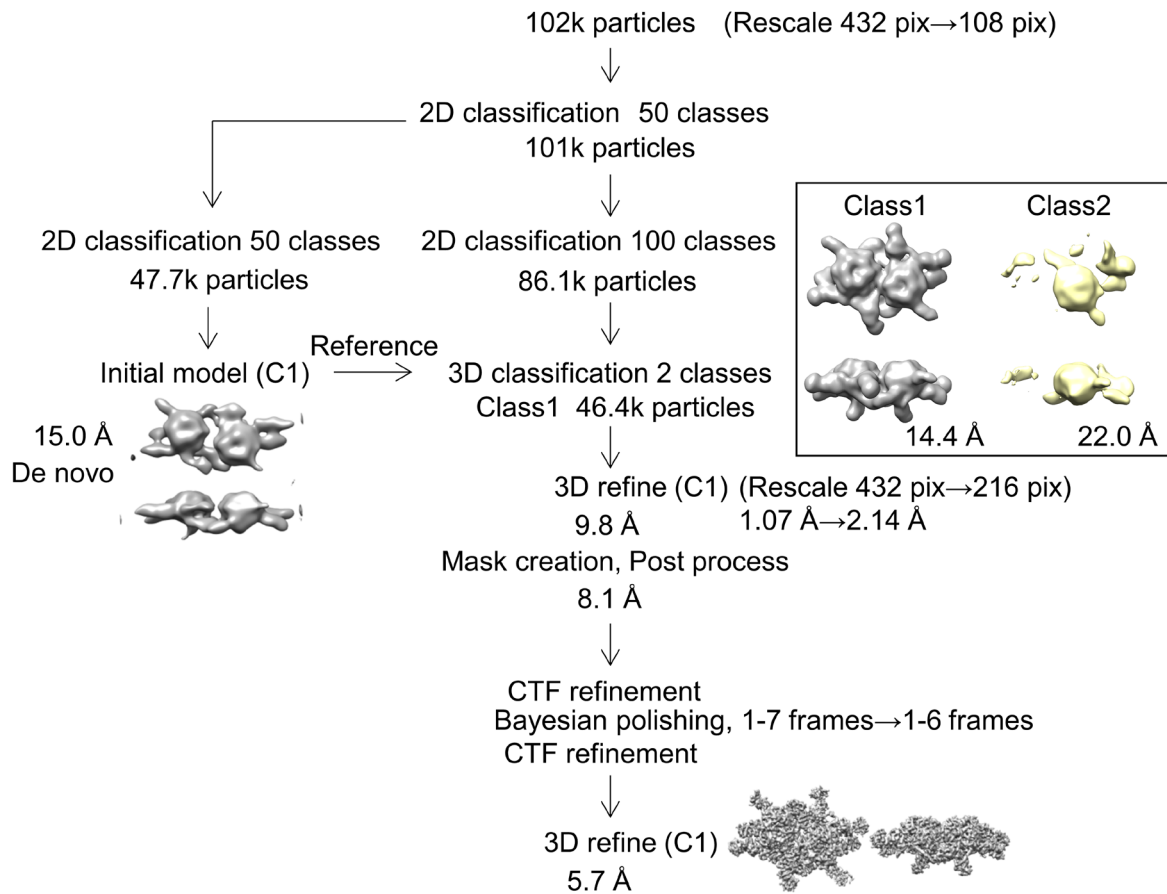


FIGURE II-2. Image process procedure for dimer cryoEM analysis. Images were analyzed by RELION3.0. Resolutions are based on the gold-standard Fourier shell correlation (FSC) = 0.143.

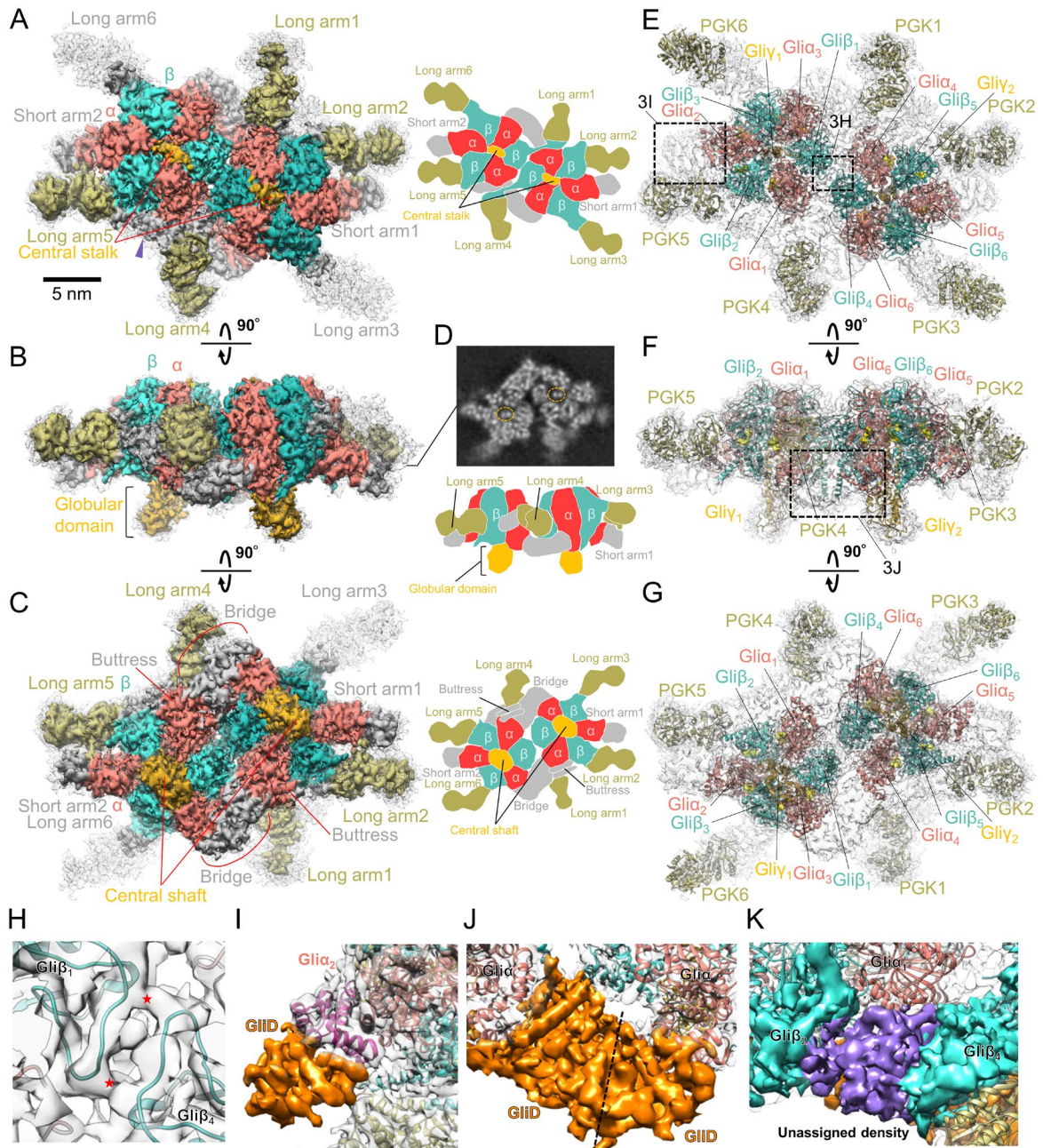


FIGURE II-3. Structure of dimer by cryoEM. (A–C) Dimer cryoEM map. Threshold levels: mesh (gray), 0.03σ ; solid, 1.15σ . In the density rendered as a solid surface, the subunits are colored. Subunits corresponding to gray solid surface were unidentified. Each illustration was depicted on the right side. (D) Cross-section through dimer cryoEM map as indicated in panel B. Coiled-coil domains in the hexamers were marked by broken lines. (E–F) Atomic model of dimer. Subunits were fitted into cryoEM map by molecular dynamics flexible fitting. (H) Interaction between hexamers. The broken boxed area in panel E was magnified. Possible interaction points were marked by asterisks. (I) Interaction between GliD and Gli α_2 . The area is marked in panel E. (J) Interaction between two GliD. The area is marked in panel F. (K) Unassigned density surrounded by Gli α_1 and the bulge structures of Gli β_2 and Gli β_4 . The area is marked in panel A as a purple triangle.

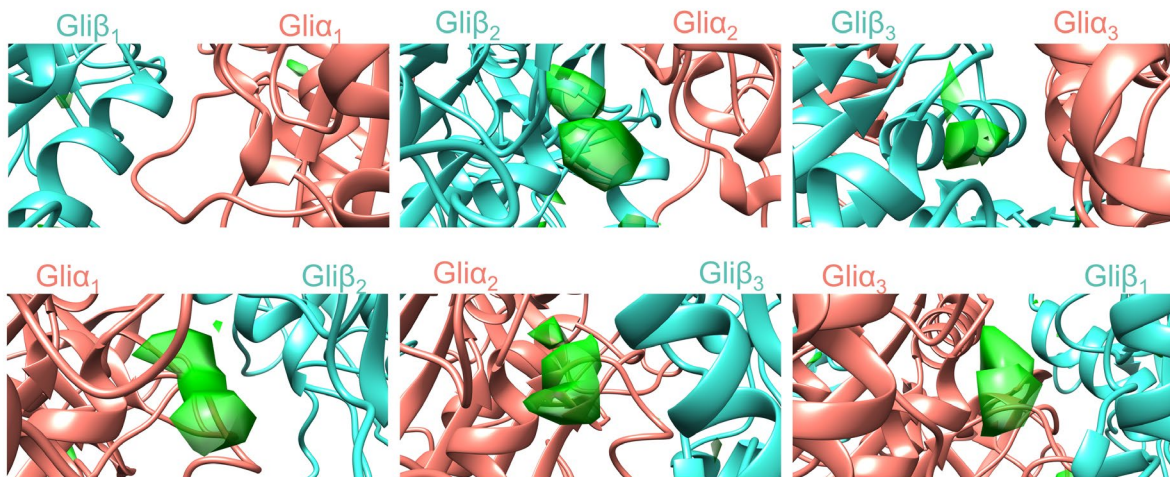


FIGURE II-4. Small molecule density at nucleotide-binding site of Gli $\alpha\beta$. Gli $\alpha\beta$ dimers have density corresponding to small molecule at catalytic site except for Gli $\alpha_1\beta_1$ dimer shown in left upper panel. Subtracted cryoEM map is colored green.

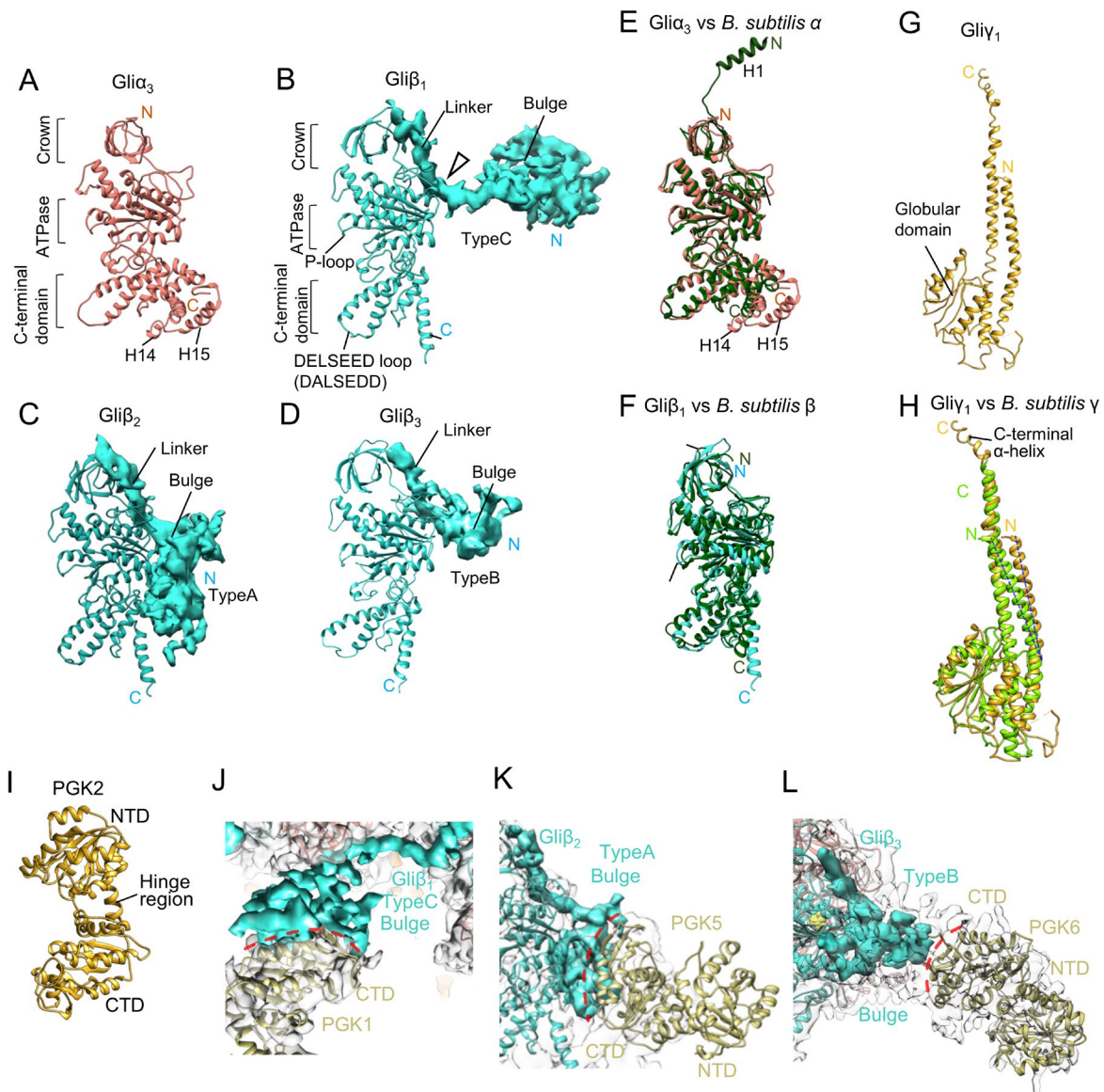


FIGURE II-5. Subunit structures. (A) Gli α_3 structure. (B-D) Gli $\beta_{1,3}$ structures. Bending point of the linker of Gli β_1 is marked by an open triangle. (E) Overlay of Gli α_3 with *Bacillus* α subunit (green; PDB ID 6N2Y) (F) Overlay of Gli β_1 with *Bacillus* SP3 β subunit (green; PDB ID 6N2Y) (G) Gli γ_1 structure. (H) Overlay of Gli γ_1 with *Bacillus* SP3 γ subunit (green; PDB ID 6N2Y) (I) Atomic model of PGK2. (J-L) All Bulge domains of Gli β subunits interacted with CTD of PGKs. Interactions between the bulge domain and CTD of PGK are marked by red broken lines.

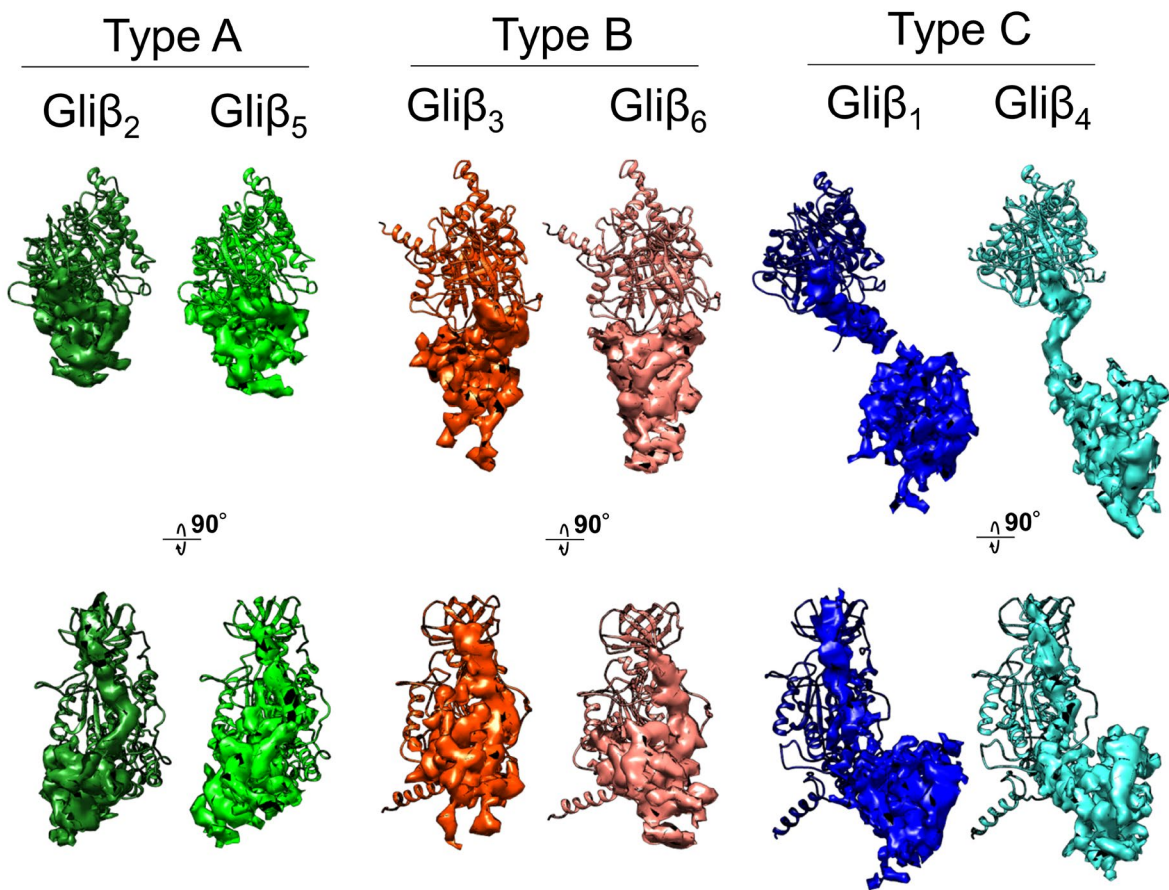


FIGURE II-6. Three types of structure composed of linker and bulge. The linker and bulge of all six Gliβ subunits were divided into three types based on their structural features.

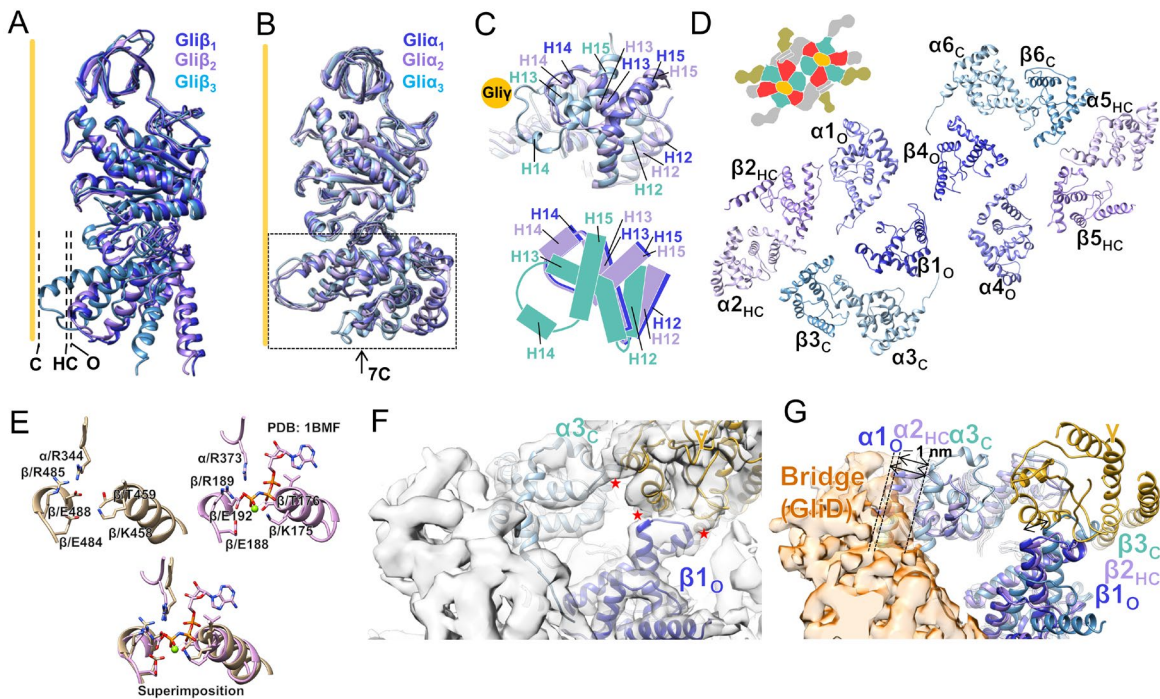


FIGURE II-7. Structural differences in hexamer. (A) Superposition of $\text{Gli}\beta_{1-3}$. A gold line indicates $\text{Gli}\gamma$ side. C-terminal positions for Closed (C), Half-Closed (HC), and Open (O) are marked by broken lines, respectively. (B) Superposition of $\text{Gli}\alpha_{1-3}$. A gold line indicates $\text{Gli}\gamma$ side. (C) Superposition of C-terminus of $\text{Gli}\alpha_{1-3}$. The broken boxed area in panel B was viewed from an arrow direction. The illustration was depicted on the lower side. (D) Asymmetrical features in C-terminal domains of hexamers. (E) Comparison of nucleotide-binding site between dimer and bovine $\text{F}_1\text{-ATPase}$ (PDB ID 1BMF) (11). The sites were superimposed by using program Fit in map in Chimera software. (F) Hexamer- $\text{Gli}\gamma$ interaction. $\text{Gli}\alpha_c$ and $\text{Gli}\beta_o$ interacted with the globular domain of $\text{Gli}\gamma$. (G) Transition simulation of $\text{Gli}\alpha\beta$. Double-head arrows indicate the distances of expected movements.

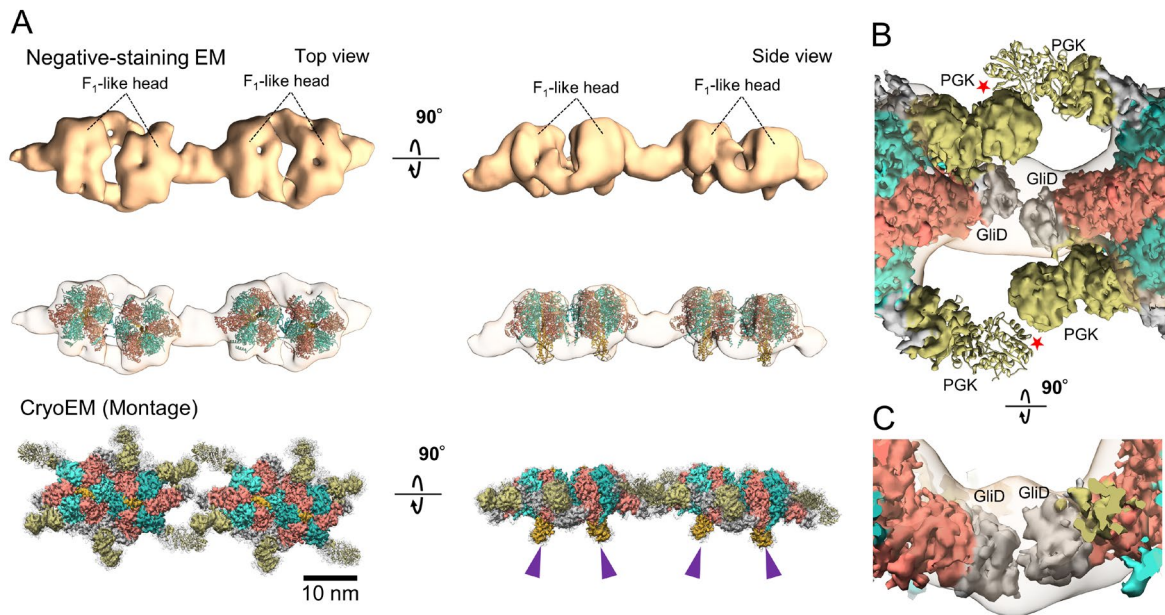


FIGURE II-8. Connection between dimers to form chain structure. (A) Comparison between dimer cryoEM map and chain 3D map. Upper: Chain 3D map obtained by negative-stain EM as shown in Fig. I-11. Middle: Atomic models of dimer reconstructed by cryoEM were fitted into 3D chain map by using program Fit in map in Chimera software. Lower: Montage chain image by cryoEM maps was created based on the positions of the atomic models as shown in the middle panel. (B-C) Dimer interface. CryoEM montage fitted into chain density map is shown here. Possible interactions are marked by asterisks.

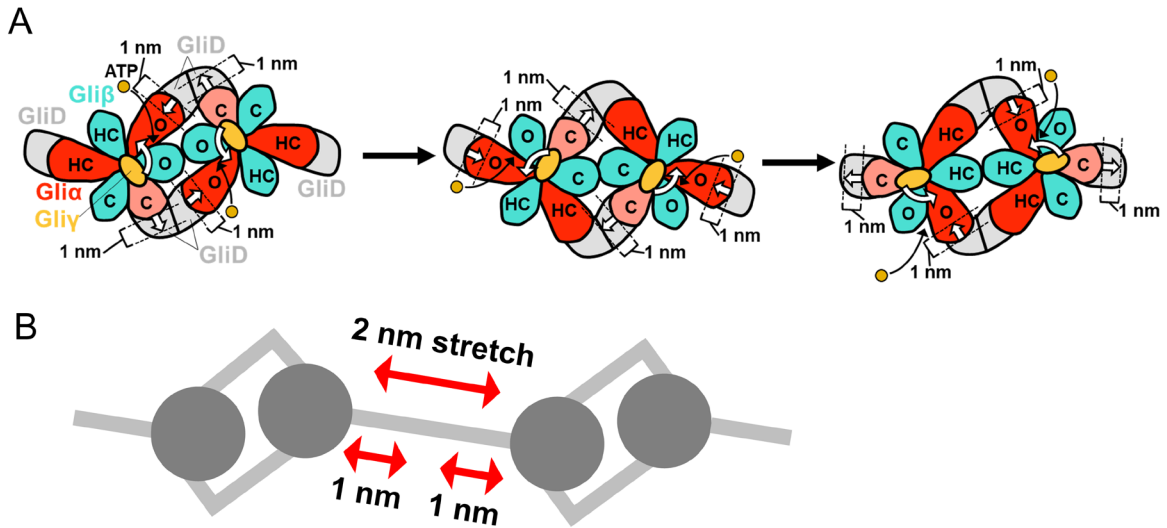


FIGURE II-9. Model for dimer movement. (A) Possible rotary catalytic mechanism of dimer. Closed, Half-Closed, and Open states of Gli $\alpha\beta$ are labelled as “C”, “HC”, and “O”, respectively. ATP is represented by an orange sphere. White arrows indicate movements. Gli α subunits push and pull GliD by approximately 1 nm. (B) Possible chain movement. Red arrows indicate movement by dimer. Each 1 nm movement by two dimer results in a 2 nm stretching motion.

CONCLUSIONS

In this thesis, I elucidated the detailed structure of the Type2-ATPase motor for *M. mobile* gliding. The structure shows both common and novel features as F₁-ATPase relatives, which will lead to understanding of the diversity of ATP synthases and the rotary catalytic mechanism. I also proposed a model for the force generation and transmission mechanism for *M. mobile* gliding. To validate these models, information on the interaction between motor and surface structures is needed, and the high-resolution visualization by cryoEM and HS-AFM studies would be critical. I discussed the development of *M. mobile* gliding from accidental contact between ATP synthase and adhesin. This idea will be important in considering the evolution of all motilities.

ACKNOWLEDGMENTS

I would like to express my hearty thanks to Prof. Makoto Miyata, Prof. Taro Nakamura, Dr. Tasuku Hamaguchi, Prof. Toshiaki Arata, Prof. Ikuko Fujiwara and Prof. Chikashi Shimoda for their elaborated guidance, invaluable criticism, and considerable encouragement. Especially, I would like to express my sincere gratitude to Prof. Makoto Miyata for providing me this precious study opportunity. I would like to thank Prof. Keiichi Namba, Prof. Takayuki Kato and Dr. Akihiro Kawamoto at Osaka University, for their valuable cooperation in cryoEM experiment and Prof. Noriyuki Kodera at Kanazawa University for his variable cooperation in HS-AFM experiment. I also thank Keisuke Kawakami at SPring-8 for giving me knowledge and advice about structural analyses, and Mr. Yuhei O Tahara at Osaka City University for technical assistance with negative-staining EM. I am deeply grateful to Prof. Ryoji Masui for his critical review of the thesis. I also thank all members of Cell Function Laboratory for discussion and giving me a lot of invaluable ideas.

Finally, I would like to extend my indebtedness to my family for their understanding, support, and encouragement throughout my study.

Funding

These works were supported by a Grant-in-Aid for Scientific Research on the Innovative Area “Harmonized Supramolecular Motility Machinery and Its Diversity”

(MEXT KAKENHI Grant Number JP24117002), by a Grants-in-Aid for Scientific Research (B) and (A) (MEXT KAKENHI Grant Numbers JP24390107, JP17H01544), by JST CREST Grant Number JPMJCR19S5, Japan, by the Osaka City University (OCU) Strategic Research Grant 2018 for top priority researches and by a Grant-in-aid of the FUGAKU TRUST FOR MEDICINAL RESEARCH to M. Miyata, and JSPS KAKENHI (Grant Number JP25000013), the Platform Project for Supporting Drug Discovery and Life Science Research (BINDS) from AMED (Grant Number JP19am0101117 and support number 1282), CiCLE (Grant Number JP17pc0101020), and JEOL YOKOGUSHI Research Alliance Laboratories of Osaka University to K. Namba.

REFERENCES

1. Weisburg WG, Tully JG, Rose DL, Petzel JP, Oyaizu H, Yang D, Mandelco L, Sechrest J, Lawrence TG, Van Etten J, et al. 1989. A phylogenetic analysis of the mycoplasmas: basis for their classification. *J Bacteriol* 171:6455-67.
2. Citti C, Dordet-Frisoni E, Nouvel LX, Kuo CH, Baranowski E. 2018. Horizontal Gene Transfers in Mycoplasmas (Mollicutes). *Curr Issues Mol Biol* 29:3-22.
3. Razin S, Yogev D, Naot Y. 1998. Molecular biology and pathogenicity of mycoplasmas. *Microbiol Mol Biol Rev* 62:1094-156.
4. Miyata M. 2010. Unique centipede mechanism of *Mycoplasma* gliding. *Annu Rev Microbiol* 64:519-37.
5. Miyata M, Hamaguchi T. 2016. Prospects for the gliding mechanism of *Mycoplasma mobile*. *Curr Opin Microbiol* 29:15-21.
6. Miyata M, Hamaguchi T. 2016. Integrated information and prospects for gliding mechanism of the pathogenic bacterium *Mycoplasma pneumoniae*. *Front Microbiol* 7:960.
7. Miyata M, Robinson RC, Uyeda TQP, Fukumori Y, Fukushima SI, Haruta S, Homma M, Inaba K, Ito M, Kaito C, Kato K, Kenri T, Kinoshita Y, Kojima S, Minamino T, Mori H, Nakamura S, Nakane D, Nakayama K, Nishiyama M, Shibata S, Shimabukuro K, Tamakoshi M, Taoka A, Tashiro Y, Tulum I, Wada H, Wakabayashi KI. 2020. Tree of motility - A proposed history of motility systems in the tree of life. *Genes Cells* 25:6-21.
8. Errington J, Mickiewicz K, Kawai Y, Wu LJ. 2016. L-form bacteria, chronic

diseases and the origins of life. *Philos Trans R Soc Lond B Biol Sci* 371:20150494.

9. Nishikawa M, Nakane D, Toyonaga T, Kawamoto A, Kato T, Namba K, Miyata M. 2019. Refined mechanism of *Mycoplasma mobile* gliding based on structure, ATPase activity, and sialic acid binding of machinery. *mBio* 10:e02846-19.
10. Kobayashi K, Kodera N, Kasai T, Tahara YO, Toyonaga T, Mizutani M, Fujiwara I, Ando T, Miyata M. 2021. Movements of *Mycoplasma mobile* gliding machinery detected by high-speed atomic force microscopy. *mBio* doi:10.1128/mBio.00040-21:e0004021.
11. Abrahams JP, Leslie AG, Lutter R, Walker JE. 1994. Structure at 2.8 Å resolution of F₁-ATPase from bovine heart mitochondria. *Nature* 370:621-8.
12. Kühlbrandt W. 2019. Structure and Mechanisms of F-Type ATP Synthases. *Annu Rev Biochem* 88:515-49.
13. Noji H, Yasuda R, Yoshida M, Kinosita K, Jr. 1997. Direct observation of the rotation of F₁-ATPase. *Nature* 386:299-302.
14. Noji H, Ueno H, McMillan DGG. 2017. Catalytic robustness and torque generation of the F₁-ATPase. *Biophys Rev* 9:103-18.
15. Beven L, Charenton C, Dautant A, Bouyssou G, Labroussaa F, Skolleremo A, Persson A, Blanchard A, Sirand-Pugnet P. 2012. Specific evolution of F₁-like ATPases in mycoplasmas. *PLoS One* 7:e38793.
16. Tulum I, Kimura K, Miyata M. 2020. Identification and sequence analyses of

- the gliding machinery proteins from *Mycoplasma mobile*. Sci Rep 10:3792.
17. Nottelet P, Bataille L, Gourgues G, Anger R, Lartigue C, Sirand-Pugnet P, Marza E, Fronzes R, Arfi Y. 2021. The mycoplasma surface proteins MIB and MIP promote the dissociation of the antibody-antigen interaction. Sci Adv 7:eabf2403.
 18. Uenoyama A, Kusumoto A, Miyata M. 2004. Identification of a 349-kilodalton protein (Gli349) responsible for cytoadherence and glass binding during gliding of *Mycoplasma mobile*. J Bacteriol 186:1537-45.
 19. Seto S, Uenoyama A, Miyata M. 2005. Identification of a 521-kilodalton protein (Gli521) involved in force generation or force transmission for *Mycoplasma mobile* gliding. J Bacteriol 187:3502-10.
 20. Uenoyama A, Miyata M. 2005. Identification of a 123-kilodalton protein (Gli123) involved in machinery for gliding motility of *Mycoplasma mobile*. J Bacteriol 187:5578-84.
 21. Uenoyama A, Seto S, Nakane D, Miyata M. 2009. Regions on Gli349 and Gli521 protein molecules directly involved in movements of *Mycoplasma mobile* gliding machinery, suggested by use of inhibitory antibodies and mutants. J Bacteriol 191:1982-5.
 22. Kusumoto A, Seto S, Jaffe JD, Miyata M. 2004. Cell surface differentiation of *Mycoplasma mobile* visualized by surface protein localization. Microbiology 150:4001-8.
 23. Miyata M, Petersen JD. 2004. Spike structure at the interface between gliding

- Mycoplasma mobile* cells and glass surfaces visualized by rapid-freeze-and-fracture electron microscopy. J Bacteriol 186:4382-6.
24. Adan-Kubo J, Uenoyama A, Arata T, Miyata M. 2006. Morphology of isolated Gli349, a leg protein responsible for *Mycoplasma mobile* gliding via glass binding, revealed by rotary shadowing electron microscopy. J Bacteriol 188:2821-8.
 25. Lesoil C, Nonaka T, Sekiguchi H, Osada T, Miyata M, Afrin R, Ikai A. 2010. Molecular shape and binding force of *Mycoplasma mobiles* leg protein Gli349 revealed by an AFM study. Biochem Biophys Res Commun 391:1312-7.
 26. Metsugi S, Uenoyama A, Adan-Kubo J, Miyata M, Yura K, Kono H, Go N. 2005. Sequence analysis of the gliding protein Gli349 in *Mycoplasma mobile*. Biophysics (Nagoya-shi) 1:33-43.
 27. Hamaguchi T, Kawakami M, Furukawa H, Miyata M. 2019. Identification of novel protein domain for sialyloligosaccharide binding essential to *Mycoplasma mobile* gliding. FEMS Microbiol Lett 366:fnz016.
 28. Morio H, Kasai T, Miyata M. 2016. Gliding direction of *Mycoplasma mobile*. J Bacteriol 198:283-90.
 29. Kasai T, Hamaguchi T, Miyata M. 2015. Gliding motility of *Mycoplasma mobile* on uniform oligosaccharides. J Bacteriol 197:2952-7.
 30. Kasai T, Nakane D, Ishida H, Ando H, Kiso M, Miyata M. 2013. Role of binding in *Mycoplasma mobile* and *Mycoplasma pneumoniae* gliding analyzed through inhibition by synthesized sialylated compounds. J Bacteriol 195:429-

- 35.
31. Nagai R, Miyata M. 2006. Gliding motility of *Mycoplasma mobile* can occur by repeated binding to *N*-acetylneuraminyllactose (sialyllactose) fixed on solid surfaces. *J Bacteriol* 188:6469-75.
32. Chen J, Neu J, Miyata M, Oster G. 2009. Motor-substrate interactions in *Mycoplasma* motility explains non-Arrhenius temperature dependence. *Biophys J* 97:2930-8.
33. Mizutani M, Tulum I, Kinoshita Y, Nishizaka T, Miyata M. 2018. Detailed analyses of stall force generation in *Mycoplasma mobile* gliding. *Biophys J* 114:1411-9.
34. Nakane D, Miyata M. 2007. Cytoskeletal "jellyfish" structure of *Mycoplasma mobile*. *Proc Natl Acad Sci U S A* 104:19518-23.
35. Tulum I, Yabe M, Uenoyama A, Miyata M. 2014. Localization of P42 and F₁-ATPase alpha-subunit homolog of the gliding machinery in *Mycoplasma mobile* revealed by newly developed gene manipulation and fluorescent protein tagging. *J Bacteriol* 196:1815-24.
36. Walker JE, Saraste M, Runswick MJ, Gay NJ. 1982. Distantly related sequences in the alpha- and beta-subunits of ATP synthase, myosin, kinases and other ATP-requiring enzymes and a common nucleotide binding fold. *EMBO J* 1:945-51.
37. Uenoyama A, Miyata M. 2005. Gliding ghosts of *Mycoplasma mobile*. *Proc Natl Acad Sci USA* 102:12754-8.

38. Kinoshita Y, Nakane D, Sugawa M, Masaike T, Mizutani K, Miyata M, Nishizaka T. 2014. Unitary step of gliding machinery in *Mycoplasma mobile*. Proc Natl Acad Sci U S A 111:8601-6.
39. Miyata M, Yamamoto H, Shimizu T, Uenoyama A, Citti C, Rosengarten R. 2000. Gliding mutants of *Mycoplasma mobile*: relationships between motility and cell morphology, cell adhesion and microcolony formation. Microbiology 146:1311-20.
40. Aluotto BB, Wittler RG, Williams CO, Faber JE. 1970. Standardized bacteriologic techniques for the characterization of *Mycoplasma* species. Int J Syst Bacteriol 20:35-58.
41. Kawakita Y, Kinoshita M, Furukawa Y, Tulum I, Tahara YO, Katayama E, Namba K, Miyata M. 2016. Structural study of MPN387, an essential protein for gliding motility of a human-pathogenic bacterium, *Mycoplasma pneumoniae*. J Bacteriol 198:2352-9.
42. Lee C, Levin A, Branton D. 1987. Copper staining: a five-minute protein stain for sodium dodecyl sulfate-polyacrylamide gels. Anal Biochem 166:308-12.
43. Dzandu JK, Johnson JF, Wise GE. 1988. Sodium dodecyl sulfate-gel electrophoresis: staining of polypeptides using heavy metal salts. Anal Biochem 174:157-67.
44. Zerbetto E, Vergani L, Dabbeni-Sala F. 1997. Quantification of muscle mitochondrial oxidative phosphorylation enzymes via histochemical staining of blue native polyacrylamide gels. Electrophoresis 18:2059-64.

45. Wittig I, Schägger H. 2005. Advantages and limitations of clear-native PAGE. *Proteomics* 5:4338-46.
46. Webb MR. 1992. A continuous spectrophotometric assay for inorganic phosphate and for measuring phosphate release kinetics in biological systems. *Proc Natl Acad Sci U S A* 89:4884-7.
47. Zhang K. 2016. Gctf: Real-time CTF determination and correction. *J Struct Biol* 193:1-12.
48. Zivanov J, Nakane T, Forsberg BO, Kimanius D, Hagen WJ, Lindahl E, Scheres SH. 2018. New tools for automated high-resolution cryo-EM structure determination in RELION-3. *eLife* 7:e42166.
49. Pettersen EF, Goddard TD, Huang CC, Couch GS, Greenblatt DM, Meng EC, Ferrin TE. 2004. UCSF Chimera--a visualization system for exploratory research and analysis. *J Comput Chem* 25:1605-12.
50. Guo H, Suzuki T, Rubinstein JL. 2019. Structure of a bacterial ATP synthase. *eLife* 8:e43128.
51. Ando T, Kodera N, Takai E, Maruyama D, Saito K, Toda A. 2001. A high-speed atomic force microscope for studying biological macromolecules. *Proc Natl Acad Sci U S A* 98:12468-72.
52. Uchihashi T, Kodera N, Ando T. 2012. Guide to video recording of structure dynamics and dynamic processes of proteins by high-speed atomic force microscopy. *Nat Protoc* 7:1193-206.
53. Ngo KX, Kodera N, Katayama E, Ando T, Uyeda TQ. 2015. Cofilin-induced

- unidirectional cooperative conformational changes in actin filaments revealed by high-speed atomic force microscopy. *eLife* 4:e04806.
54. Bowler MW, Montgomery MG, Leslie AG, Walker JE. 2006. How azide inhibits ATP hydrolysis by the F-ATPases. *Proc Natl Acad Sci U S A* 103:8646-9.
 55. Ando T. 2018. High-speed atomic force microscopy and its future prospects. *Biophys Rev* 10:285-92.
 56. Uchihashi T, Iino R, Ando T, Noji H. 2011. High-speed atomic force microscopy reveals rotary catalysis of rotorless F₁-ATPase. *Science* 333:755-8.
 57. Cheng Y, Wolf E, Larvie M, Zak O, Aisen P, Grigorieff N, Harrison SC, Walz T. 2006. Single particle reconstructions of the transferrin-transferrin receptor complex obtained with different specimen preparation techniques. *J Mol Biol* 355:1048-65.
 58. Dibrova DV, Konovalov KA, Perekhvatov VV, Skulachev KV, Mulkidjanian AY. 2017. COGcollator: a web server for analysis of distant relationships between homologous protein families. *Biol Direct* 12:29.
 59. Neuwald AF, Aravind L, Spouge JL, Koonin EV. 1999. AAA+: A class of chaperone-like ATPases associated with the assembly, operation, and disassembly of protein complexes. *Genome Res* 9:27-43.
 60. Snider J, Thibault G, Houry WA. 2008. The AAA+ superfamily of functionally diverse proteins. *Genome Biol* 9:216.
 61. Minauro-Sanmiguel F, Wilkens S, García JJ. 2005. Structure of dimeric

- mitochondrial ATP synthase: novel F₀ bridging features and the structural basis of mitochondrial cristae biogenesis. *Proc Natl Acad Sci U S A* 102:12356-8.
62. Allegretti M, Klusch N, Mills DJ, Vonck J, Kühlbrandt W, Davies KM. 2015. Horizontal membrane-intrinsic α -helices in the stator a-subunit of an F-type ATP synthase. *Nature* 521:237-40.
63. Blum TB, Hahn A, Meier T, Davies KM, Kühlbrandt W. 2019. Dimers of mitochondrial ATP synthase induce membrane curvature and self-assemble into rows. *Proc Natl Acad Sci U S A* 116:4250-4255.
64. Naito TM, Masaike T, Nakane D, Sugawa M, Okada KA, Nishizaka T. 2019. Single-molecule pull-out manipulation of the shaft of the rotary motor F₁-ATPase. *Sci Rep* 9:7451.
65. Watson HC, Walker NP, Shaw PJ, Bryant TN, Wendell PL, Fothergill LA, Perkins RE, Conroy SC, Dobson MJ, Tuite MF. 1982. Sequence and structure of yeast phosphoglycerate kinase. *EMBO J* 1:1635-40.
66. Jaffe JD, Stange-Thomann N, Smith C, DeCaprio D, Fisher S, Butler J, Calvo S, Elkins T, FitzGerald MG, Hafez N, Kodira CD, Major J, Wang S, Wilkinson J, Nicol R, Nusbaum C, Birren B, Berg HC, Church GM. 2004. The complete genome and proteome of *Mycoplasma mobile*. *Genome Res* 14:1447-61.
67. Lu M, Holliday LS, Zhang L, Dunn WA, Jr., Gluck SL. 2001. Interaction between aldolase and vacuolar H⁺-ATPase: evidence for direct coupling of glycolysis to the ATP-hydrolyzing proton pump. *J Biol Chem* 276:30407-13.

68. Lu M, Ammar D, Ives H, Albrecht F, Gluck SL. 2007. Physical interaction between aldolase and vacuolar H⁺-ATPase is essential for the assembly and activity of the proton pump. *J Biol Chem* 282:24495-503.
69. Chan CY, Dominguez D, Parra KJ. 2016. Regulation of Vacuolar H⁺-ATPase (V-ATPase) Reassembly by Glycolysis Flow in 6-Phosphofructo-1-kinase (PFK-1)-deficient Yeast Cells. *J Biol Chem* 291:15820-9.
70. Kinoshita Y, Miyata M, Nishizaka T. 2018. Linear motor driven-rotary motion of a membrane-permeabilized ghost in *Mycoplasma mobile*. *Sci Rep* 8:11513.
71. Nogales E, Scheres SH. 2015. Cryo-EM: A Unique Tool for the Visualization of Macromolecular Complexity. *Mol Cell* 58:677-89.
72. Yip KM, Fischer N, Paknia E, Chari A, Stark H. 2020. Atomic-resolution protein structure determination by cryo-EM. *Nature* 587:157-61.
73. Skiniotis G, Southworth DR. 2016. Single-particle cryo-electron microscopy of macromolecular complexes. *Microscopy (Oxf)* 65:9-22.
74. Zivanov J, Nakane T, Scheres SHW. 2019. A Bayesian approach to beam-induced motion correction in cryo-EM single-particle analysis. *IUCrJ* 6:5-17.
75. Kim DE, Chivian D, Baker D. 2004. Protein structure prediction and analysis using the Robetta server. *Nucleic Acids Res* 32:W526-31.
76. Stocker A, Keis S, Vonck J, Cook GM, Dimroth P. 2007. The structural basis for unidirectional rotation of thermoalkaliphilic F₁-ATPase. *Structure* 15:904-14.
77. Kabaleeswaran V, Shen H, Symersky J, Walker JE, Leslie AG, Mueller DM.

2009. Asymmetric structure of the yeast F1 ATPase in the absence of bound nucleotides. *J Biol Chem* 284:10546-51.
78. Morales-Rios E, Montgomery MG, Leslie AG, Walker JE. 2015. Structure of ATP synthase from *Paracoccus denitrificans* determined by X-ray crystallography at 4.0 Å resolution. *Proc Natl Acad Sci U S A* 112:13231-6.
79. Lee JH, Im YJ, Bae J, Kim D, Kim MK, Kang GB, Lee DS, Eom SH. 2006. Crystal structure of *Thermus caldophilus* phosphoglycerate kinase in the open conformation. *Biochem Biophys Res Commun* 350:1044-9.
80. Chacón P, Wriggers W. 2002. Multi-resolution contour-based fitting of macromolecular structures. *J Mol Biol* 317:375-84.
81. Trabuco LG, Villa E, Mitra K, Frank J, Schulten K. 2008. Flexible fitting of atomic structures into electron microscopy maps using molecular dynamics. *Structure* 16:673-83.
82. Emsley P, Cowtan K. 2004. Coot: model-building tools for molecular graphics. *Acta Crystallogr D Biol Crystallogr* 60:2126-32.
83. Adams PD, Grosse-Kunstleve RW, Hung LW, Ioerger TR, McCoy AJ, Moriarty NW, Read RJ, Sacchettini JC, Sauter NK, Terwilliger TC. 2002. PHENIX: building new software for automated crystallographic structure determination. *Acta Crystallogr D Biol Crystallogr* 58:1948-54.
84. Cianfrocco MA, DeSantis ME, Leschziner AE, Reck-Peterson SL. 2015. Mechanism and regulation of cytoplasmic dynein. *Annu Rev Cell Dev Biol* 31:83-108.

85. Erickson HP. 2009. Size and shape of protein molecules at the nanometer level determined by sedimentation, gel filtration, and electron microscopy. Biol Proced Online 11:32-51.